Diploma Thesis

Czech Technical University in Prague

F3

Faculty of Electrical Engineering
Department of Electromagnetic Field

Design and Optimization of Multi-port Antenna

Vojtěch Neuman

Supervisor: Doc. Ing. Miloslav Čapek Ph.D.
Supervisor–specialist: Doc. Ing. Lukáš Jelínek Ph.D.
Field of study: Electronics and Communications
Subfield: Radio Systems
May 2021

ZADÁNÍ DIPLOMOVÉ PRÁCE

I. OSOBNÍ A STUDIJNÍ ÚDAJE

Příjmení: **Neuman** Jméno: **Vojtěch** Osobní číslo: **465820**

Fakulta/ústav: **Fakulta elektrotechnická**

Zadávající katedra/ústav: **Katedra elektromagnetického pole**

Studijní program: **Elektronika a komunikace**

Specializace: **Rádiové komunikace a systémy**

II. ÚDAJE K DIPLOMOVÉ PRÁCI

Název diplomové práce:

Návrh a optimalizace víceportových antén

Název diplomové práce anglicky:

Design and Optimization of Multi-port Antenna

Pokyny pro vypracování:

Consider an antenna in a form of a metallic rim with a parasitic ground plane with dimensions typical for a smart-phone's chassis [1]. Treat the antenna as a multi-port element and assume a lossy material (copper).
Summarize important antenna design parameters (fractional bandwidth, total active reflection coefficient, radiation efficiency, electrical size, realized gain, capacity) and methods to optimize them. Use method of moments [2] both for analysis and optimization. Express all used physical quantities in a port basis [3].
Perform feeding synthesis, searching for optimal number of ports, their placement, and feeding amplitude and phase, considering various designing criteria defined above.
Discuss possibilities to match the ports and construct realistic feeding network. Consider matching via parallel-connected ideal matching element as well as by a general multi-port circuit.
Verify the model optimized in AToM [4] in a commercial EM simulator CST [5], consider dielectric posts required for manufacturing, and describe how they influence the optimized results. Propose realistic feeding and evaluate its influence on the original results. Finally, describe the manufacturing process and discuss how to improve the feeding synthesis procedure to better match realistic multi-port antenna design.

Seznam doporučené literatury:

[1] Luomaniemi, R., Hannula, J.-M., Lehtovuori, A., Viikari, V.: Switch-Reconfigurable Metal Rim MIMO Handset Antenna With Distributed Feeding, IEEE Access, Vol. 7, pp. 48971-48981, 2019.
[2] Harrington, R. F.: Field Computation by Moment Methods, Wiley - IEEE Press, 1993.
[3] Capek, M., Jelinek, L., Masek, M.: Finding Optimal Total Active Reflection Coefficient and Realized Gain for Multi-port Lossy Antennas, pp. 1-13, 2020. arxiv: https://arxiv.org/abs/2002.12747
[4] CTU in Prague, Antenna Toolbox for MATLAB (AToM), [on-line: www.antennatoolbox.com, accessed: 03-10-2020].
[5] Dassault Systemes, CST Studio Suite, [on-line: https://www.3ds.com/products-services/simulia/products/cst-studio-suite/, accessed: 03-10-2020].

Jméno a pracoviště vedoucí(ho) diplomové práce:

doc. Ing. Miloslav Čapek, Ph.D., katedra elektromagnetického pole FEL

Jméno a pracoviště druhé(ho) vedoucí(ho) nebo konzultanta(ky) diplomové práce:

Datum zadání diplomové práce: **09.02.2021** Termín odevzdání diplomové práce: **21.05.2021**

Platnost zadání diplomové práce: **30.09.2022**

doc. Ing. Miloslav Čapek, Ph.D. podpis vedoucí(ho) práce	podpis vedoucí(ho) ústavu/katedry	prof. Mgr. Petr Páta, Ph.D. podpis děkana(ky)

III. PŘEVZETÍ ZADÁNÍ

Diplomant bere na vědomí, že je povinen vypracovat diplomovou práci samostatně, bez cizí pomoci, s výjimkou poskytnutých konzultací.
Seznam použité literatury, jiných pramenů a jmen konzultantů je třeba uvést v diplomové práci.

. _____
Datum převzetí zadání

_____
Podpis studenta

Acknowledgements

I would like to thank my mother and father for everything they have done for me in these hard times. Words cannot express my gratitude towards my mentors Miloslav Capek and Lukas Jelinek, for all help and advice I have received from them through the years. I would like to thank Jan Spacil for his priceless help with physical realization and measurements. I also have to mention all my friends, especially the so-called group FEL*i*ta, and thank them for making my life better and happier. And I would like to express my acknowledgment to my friend Richard, that he never gave me up and that he never let me down.

Declaration

I declare that I have written submitted thesis by myself and that I have listed all information sources in accordance with Methodical Guideline on Compliance with Ethical Principles.

In Prague, May 21, 2021

Prohlašuji, že jsem předloženou práci vypracoval samostatně a že jsem uvedl veškeré použité informační zdroje v souladu s Metodickým pokynem o dodržování etických principů při přípravě vysokoškolských závěrečných prací.

V Praze, 21. května 2021

Abstract

This work focuses on the optimization of mobile phone antenna in the vicinity of frequency 700 MHz. The description is based on the conversion of method-of-moments matrix operators into port-mode operators reducing the degrees of freedom. Antennas are optimized with respect to minimization of total active reflection coefficient. Optimal feeding positions, optimal feeding voltage, and corresponding matching elements are found. Results are verified in commercial field simulators. Optimal designs serve as models for manufactured realistic radiators.

Keywords: Numerical methods, Computational electromagnetism, Method of moments, Convex optimization, Port modes, Electromagnetic field simulations, Matching circuits

Supervisor: Doc. Ing. Miloslav Čapek Ph.D.
Faculty of Electrical Engineering,
Technická 2,
160 00 Praha 6

Abstrakt

Práce se zaměřuje na optimalizaci antény pro mobilní telefon v pásmu 700 MHz. Popis je založen na konverzi maticových operátorů získaných metodou momentů na port-mode operátory, čímž se redukuje počet stupňů volnosti. Antény jsou optimalizovány za účelem dosažení minimálního celkového aktivního koeficientu odrazu. Optimalizace vede na nalezení optimálních pozic napájení, optimálních amplitud a fází a jim odpovídajících přizpůsobovacích prvků. Výsledky jsou ověřeny v komerčních simulátorech pole. Na základě optimálních designů jsou navržené a vyrobené reálné prototypy zářičů.

Klíčová slova: Numerické metody, Výpočetní elektromagnetismus, Metoda momentů, Konvexní optimalizace, Port mody, Simulace elektromagnetického pole, Přizpůsobovací obvody

Překlad názvu: Návrh a optimalizace víceportových antén

Contents

Figures

Tables

Chapter 1

Introduction

Today's world is represented by mutual connection and information sharing. High-quality multimedia, large data sets, intelligent sensors, and industry 4.0, augmented by virtual reality, demands high bit-rates and low latency in modern communication systems [1]. This puts extreme demands on every component of a communication chain, which must be revised to fully support all the above-mentioned features.

Nowadays, radiators carry the burden of harsh requirements on available space in modern cell phones, and spectrum is heavily occupied. Ordinary design routines are not sufficient to achieve these goals, and the final design is always a product of optimization. Design software have built-in shape optimizations procedures. However, those procedures are all based on repeated numerical simulation of modified structure, which is always time-consuming. The alternative relaxed approach is based on feeding optimization where the shape is fixed, and port placement, feeding voltages, and matching circuits are optimized. This requires only a single run of electromagnetic simulation at a single frequency.

1.1 Multi-Port Radiators

Antenna characteristics, such as gain or efficiency, are not dependent on feeding voltage for single-port antennas, which means that they lose this degree of freedom of their adjustment. Multi-port antennas, in contrast, actively employ feeding voltage, allowing, for example, beam-steering of radiation patterns [2], maximization of efficiency or gain, and others.

Design of a multi-port antenna is still a subject of extensive academic research. Some breakthroughs were already achieved with antenna cluster concept and distributed feeding [3–5], or with characteristic modes approach [6–8]. There are design and optimization problems which still do not have clear resolution.

This work compares an optimal performance of a 2-port antenna and a 1-port antenna. Optimization of feeding position is done in both cases, while optimization of feeding voltages is done only for the case of the 2-port system. The feeding optimization is extended by a design of optimal matching elements at each port, furthermore improving the total efficiency of

the antenna. Achieved results will serve as a basis for practical realization and its characterization via measurements.

1.2 Model and Methodology

Antenna model used throughout this thesis is shown in Figure 1.1. The antenna consists of a rim Ω_{A} with connected feeding and a ground plane Ω_{G}. The described antenna represents a simplified model of a standard mobile

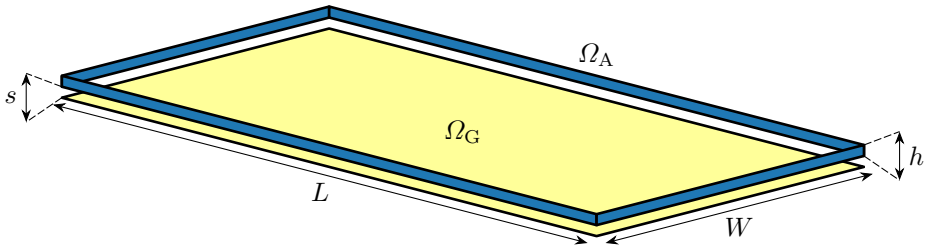

Figure 1.1: Schematic of the optimized antenna. Blue region represents a rim where feeding ports are connected. Yellow region represents a ground plane. Length and width of the antenna are $L = 150\,\mathrm{mm}$ and $W = 75\,\mathrm{mm}$, respectively. Spacing between rim and ground plane is $s = 2.25\,\mathrm{mm}$. Height of the rim is $h = 2.25\,\mathrm{mm}$.

phone chassis with a side ratio $W = L/2$. Electrical size ka in the range between 1.05 and 1.32 is to be used. This corresponds to the frequency range between 600 MHz and 750 MHz, which in the Czech Republic belong to the 2nd, 4th, and 5th generation cellular networks [9]. Only the rim of the antenna is assumed to be controllable via optimization. Lossy metal with surface conductivity $\sigma = 5.97 \cdot 10^7\,\mathrm{S/m}$ (copper) is considered for design, but dielectric supports and PCB boards existing in the real mobile phone are omitted for simplicity. The effect of those is discussed later in the chapter about physical realization.

For numerical simulations and optimization, the model is discretized into a triangular mesh grid, see Figure 1.2, consisting of 562 triangles in the ground plane and 360 triangles in the rim. Although the antenna is symmetrical, discretization does not preserve this symmetry which simplifies the evaluation of fundamental bounds[1].

Field simulations and optimization is primarily based on AToM version 1.5 [11] which uses method-of-moments formulation of electric field integral equation. It also allows for evaluating matrix operators describing field quantities that operate over current density. These MoM-like operators are subsequently rewritten to port-reduced operators, which are used to evaluate antenna figures of merit and optimize various antenna parameters.

The main results are further compared with commercial field simulator CST Studio Suite 2020 using Integral Solver [12] and matching circuits are treated with AWR Design Environment 15 [13].

[1] Symmetrical meshes bring eigenvalue crossings problem [10].

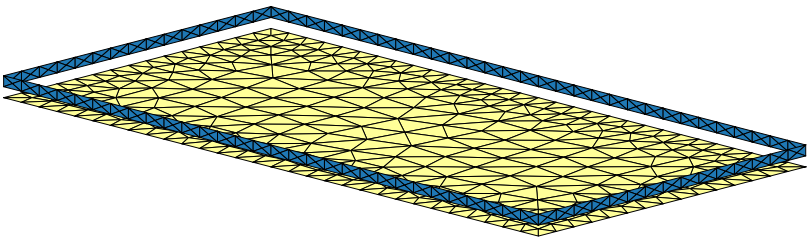

Figure 1.2: Triangular mesh of the used antenna model. The rim is discretized into a uniform mesh grid and the ground plane is discretized using Delaunay triangulation.

1.3 Goals of This Thesis

The method described here consists of several types of optimization. Feeding voltages and matching lines can be fixed as uniform, and combinatoric optimization can be performed over feeding placement. Another way is fixing matching impedances only and utilize convex optimization of feeding voltages and again find optimal feeding placement. The last level is the optimization of feeding voltages and matching circuits through nonlinear optimization and once again perform an exhaustive search of the best feeding position. Matching circuits are at first idealized with feeding line and parallel disperse tuning susceptance element, but a tool synthesizing general two-port matching circuits is presented in the latter. It is shown that two-element lumped matching circuits do not have any severe performance decrease.

This leads to systematic design workflow, which results in optimal port placement and feeding, which will serve as a basis for a more realistic simulation model for the practical realization of a simplified cellphone-resembling radiator. The manufactured model will be measured and compared in a backward manner to previous simplified models.

All antenna ports are considered to share the same frequency. The case of the multi-resonant radiator is not addressed in this work.

This work has the following goals:

1. Description of multi-port antenna parameters and their expression in a so-called port-mode basis.
2. Proposition of optimization routines and their solution for single-port and multi-port antennas.
3. Examination of more realistic feeding and matching circuits effect on the idealized case.
4. Realization of an antenna prototype and its comparison with simulation.

Each of these points will be solved separately in the following four chapters.

Chapter 2

Theoretical Background

This chapter summarizes the important theory underlying this work. Design parameters are also introduced, including their description via port-matrices obtained from full-wave operators. The theoretical developments leading to full-wave operators are left for Appendix A.

2.1 Design Parameters

This section introduces selected antenna parameters, namely:

1. *Port admittance matrix* which represents relation between voltages and currents on P antenna ports[1]

$$\begin{bmatrix} y_{11} & y_{12} & \cdots & y_{1P} \\ y_{21} & y_{22} & & y_{2P} \\ \vdots & & \ddots & \vdots \\ y_{P1} & y_{P2} & \cdots & y_{PP} \end{bmatrix} \begin{bmatrix} i_1 \\ i_2 \\ \vdots \\ i_P \end{bmatrix} = \begin{bmatrix} v_1 \\ v_2 \\ \vdots \\ v_P \end{bmatrix}, \tag{2.1}$$

with v_n and i_n being voltages and currents on the n-th port respectively. Elements of admitance matrix y_{mn} might be evaluated as [14]

$$y_{mn} = \left.\frac{i_m}{v_n}\right|_{v_j=0 \text{ for } j\neq n}. \tag{2.2}$$

The relation (2.1) is alternatively written in compact algebraic form as $\mathbf{yi} = \mathbf{v}$. Input admittance seen at the m-th port is obtained as

$$y_{\text{in},m} = \sum_{n=1}^{P} y_{mn}\frac{v_n}{v_m}. \tag{2.3}$$

2. *Total active reflection coefficient* which is a value characterising antenna's capability to radiate power delivered to its terminals [15]. It is defined as

$$\Gamma^{\text{t}} = \sqrt{1 - \frac{P_{\text{rad}}}{P_{\text{in}}}}, \tag{2.4}$$

[1] Harmonic steady-state and time convention $\partial/\partial t \to \mathrm{i}\omega$ are assumed.

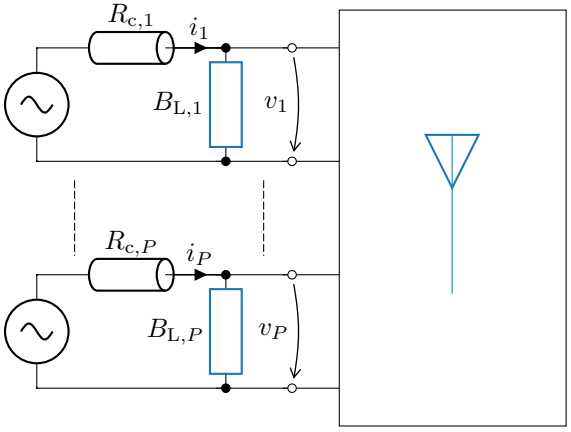

Figure 2.1: Multi-port antenna system. $R_{c,p}$ represents characteristic line impedance. Tuning elements $B_{L,p}$ match antenna ports with line.

with P_{rad} being radiated power and P_{in} denoting input power. Total active reflection coefficient Γ^t takes into account power delivered to all ports and also considers losses on antenna itself. Total active reflection coefficient reduces to reflection coefficient Γ [14] in case of a single-port lossless antenna, with Γ evaluated as

$$\Gamma = \frac{z_{in} - R_c}{z_{in} + R_c}. \tag{2.5}$$

3. *Bandwidth* B which, referring to [16], is a range of frequencies within which a performance of a device, in respect to some characteristic, conforms to a specified standard.

   Due to different frequency bands used in wireless communication, this parameter is often replaced by fractional bandwidth FBW, which better describes communication system demands. Fractional bandwidth is defined as

$$\mathrm{FBW} = 2\frac{f_2 - f_1}{f_2 + f_1}, \tag{2.6}$$

   with f_1 (respectively f_2) denoting start (respectively end) of frequency band in which some particular parameter is achieved on required level. Fractional bandwidth for multi-port antennas is determined from total active reflection coefficient Γ^t defined above. Fractional bandwidth can be alternatively evaluated with utilisation of proportional relation between fractional bandwidth and Q-factor [17], which reads

$$Q = \frac{2\omega \max\{W_e, W_m\}}{P_{rad}}, \tag{2.7}$$

   where W_e and W_m are electric and magnetic energies. This way is perfectly valid for single-port antenna systems, however, there is still lack of proof of correctness of usage of this parameter for multi-por antennas.

The inverse proportionality ratio used here is [18]

$$\mathrm{FBW} = \frac{2\sqrt{\beta}}{Q}, \tag{2.8}$$

where $\beta \in [0, 1]$ represents level of considered voltage standing wave ratio.

4. *Efficiency* which is a ratio of useful power to total power. Three different efficiencies are considered in this work. Radiation efficiency η_{rad} [17] is a ratio of the radiated power and total dissipated power

$$\eta_{\mathrm{rad}} = \frac{P_{\mathrm{rad}}}{P_{\mathrm{rad}} + P_{\mathrm{lost}}}. \tag{2.9}$$

Matching efficiency [19] is a ratio of the total dissipated power and the total input power

$$\eta_{\mathrm{match}} = \frac{P_{\mathrm{rad}} + P_{\mathrm{lost}}}{P_{\mathrm{in}}}. \tag{2.10}$$

The total efficiency is defined as a product [19]

$$\eta_{\mathrm{tot}} = \eta_{\mathrm{rad}}\eta_{\mathrm{match}} = \frac{P_{\mathrm{rad}}}{P_{\mathrm{in}}} = 1 - \left(\Gamma^{\mathrm{t}}\right)^2. \tag{2.11}$$

Analytical relation for evaluation of multi-port antenna efficiency has been already derived [20]. However, it assumes an antenna without a ground plane, and its computation is based on different total active reflection coefficient definition; therefore, it is not used in this work.

5. *Gain* which is a product of antenna directivity and efficiency. Realized gain G^{t} reads

$$G^{\mathrm{t}}\left(\hat{\boldsymbol{r}}, \hat{\boldsymbol{e}}\right) = \eta_{\mathrm{tot}} D\left(\hat{\boldsymbol{r}}, \hat{\boldsymbol{e}}\right), \tag{2.12}$$

where D is a partial directivity [21] defined as

$$D\left(\hat{\boldsymbol{r}}, \hat{\boldsymbol{e}}\right) = \frac{1}{2Z_0} \frac{\left|\hat{\boldsymbol{e}} \cdot \boldsymbol{F}\left(\hat{\boldsymbol{r}}\right)\right|^2}{P_{\mathrm{rad}}}, \tag{2.13}$$

where Z_0 is the free space impedance and F is a radiation pattern.

6. *Cross correlation coefficient* which is important MIMO antennas parameter indicating correlation of far-field patterns [6]. Elements of port correlation matrix $\boldsymbol{\Psi}$ are calculated as

$$\Psi_{mn} = \frac{\int\limits_{4\pi} \boldsymbol{F}_m\left(\hat{\boldsymbol{r}}\right) \cdot \boldsymbol{F}_n^*\left(\hat{\boldsymbol{r}}\right) \mathrm{d}\Omega}{\sqrt{\int\limits_{4\pi} \left\|\boldsymbol{F}_m\left(\hat{\boldsymbol{r}}\right)\right\|^2 \mathrm{d}\Omega} \sqrt{\int\limits_{4\pi} \left\|\boldsymbol{F}_n\left(\hat{\boldsymbol{r}}\right)\right\|^2 \mathrm{d}\Omega}}, \tag{2.14}$$

where $\boldsymbol{F}_m$ is far-field of m-th radiation pattern. Port correlation matrix $\boldsymbol{\Psi}$ is identity matrix in ideal case.

7. *Capacity* of a communication channel which represents maximum error-free data rate that a channel can support [22]. Capacity for a MIMO system with N channels reads [23]

$$C = \log_2 \det \left(\mathbf{E} + \frac{\overline{\gamma}}{N} \mathbf{H}^{\mathrm{H}} \mathbf{C} \mathbf{H} \right), \tag{2.15}$$

where $\mathbf{E} \in \mathbb{R}^{N \times N}$ is the unit matrix, $\overline{\gamma}$ is the mean signal-to-noise ratio per channel, $\mathbf{H}$ is the channel matrix and $\mathbf{C}$ is the correlation matrix for transmitted data. Capacity C represents upper bound on code rates [23].

The parameters stated above are powerful in their readability. However, their definitions are not suitable for direct evaluation. Therefore, they will be expressed in a so-called port-mode basis [24] which allows for a direct optimization.

The last two parameters are essential for the classification of MIMO antennas, however, this work does not address this problem, and therefore these two parameters are not handled in the latter.

2.2 Port Modes

This section describes transformation between MoM-like quantities and port-mode quantities [19]. This transformation is based on two relations. The first is the power conservation

$$\mathbf{I}^{\mathrm{H}} \mathbf{V} = \mathbf{i}^{\mathrm{H}} \mathbf{v}, \tag{2.16}$$

where the capital letters on the left hand side are used for MoM quantities and small letters on the right hand side are used for port quantities. The second are the matrix descriptions

$$\mathbf{Z}\mathbf{I} = \mathbf{V}, \tag{2.17}$$

$$\mathbf{z}\mathbf{i} = \mathbf{v}, \tag{2.18}$$

with $\mathbf{Z} \in \mathbb{C}^{N \times N}$ with N being the number of basis functions and with $\mathbf{z} \in \mathbb{C}^{P \times P}$ with P denoting the number of ports. It is worth noticing that physical limitation $P \ll N$ implies enormous reduction in degrees-of-freedom (DOFs) in feeding problem and speeds up optimization problems [19].

Considering that there is a voltage v impressed to a particular port, the excitation vector is written as [19]

$$\mathbf{V} = \mathbf{D}\mathbf{p}v, \tag{2.19}$$

where $\mathbf{p}$ is a vector of weights representing feeding port, the length of which is equal to the number of basis functions N. Matrix $\mathbf{D} \in \mathbb{R}^{N \times N}$ ensures correct units

$$D_{mn} = \begin{cases} \zeta_m & m = n, \\ 0 & \text{otherwise}, \end{cases} \tag{2.20}$$

where ζ_m is related to the chosen basis functions system[2].

When more ports exist, with port voltages aggregated in vector $\mathbf{v}$, the excitation vector is written as

$$\mathbf{V} = \mathbf{DPv}, \tag{2.21}$$

where matrix $\mathbf{P} = [\mathbf{p}_1, \ldots, \mathbf{p}_M]$ contains vectors $\mathbf{p}_m$ of different ports.

The total current generated by excitation (2.21) reads

$$\mathbf{I} = \mathbf{YDPv}, \tag{2.22}$$

where $\mathbf{Y} = \mathbf{Z}^{-1}$ is the admitance matrix. Port current vector $\mathbf{i}$ results from (2.22) multiplied by $\mathbf{P}^{\mathrm{H}}\mathbf{D}^{\mathrm{H}}$

$$\mathbf{i} = \mathbf{P}^{\mathrm{H}}\mathbf{D}^{\mathrm{H}}\mathbf{I} = \mathbf{P}^{\mathrm{H}}\mathbf{D}^{\mathrm{H}}\mathbf{YDPv} = \mathbf{yv}, \tag{2.23}$$

where $\mathbf{y} = \mathbf{P}^{\mathrm{H}}\mathbf{D}^{\mathrm{H}}\mathbf{YDP}$ denotes port admittance matrix. Port impedance matrix $\mathbf{z}$ is finally obtained as $\mathbf{z} = \mathbf{y}^{-1}$.

Incoming and reflected power waves amplitudes [14], $\mathbf{a}$ and $\mathbf{b}$, existing in transmission lines connected to ports are expressed as [19]

$$\mathbf{a} = \frac{1}{2}\left(\mathbf{E} + \mathbf{\Lambda}\left(\mathbf{y} + \mathbf{y}_{\mathrm{L}}\right)\mathbf{\Lambda}\right)\mathbf{\Lambda}^{-1}\mathbf{v} = \mathbf{k}_{\mathrm{i}}\mathbf{v}, \tag{2.24}$$

$$\mathbf{b} = \frac{1}{2}\left(\mathbf{E} - \mathbf{\Lambda}\left(\mathbf{y} + \mathbf{y}_{\mathrm{L}}\right)\mathbf{\Lambda}\right)\mathbf{\Lambda}^{-1}\mathbf{v} = \mathbf{k}_{\mathrm{r}}\mathbf{v}, \tag{2.25}$$

where $\mathbf{\Lambda}$ is a diagonal matrix with elements $\Lambda_{pp} = \sqrt{R_{\mathrm{c},p}}$ with $R_{\mathrm{c},p}$ being characteristic impedance of feeding line connected to the p-th port. Both (2.24) and (2.25) contain also diagonal matrix $\mathbf{y}_{\mathrm{L}} = \mathrm{i}\mathbf{b}_{\mathrm{L}}$ which represents tuning susceptance elements $\mathrm{i}B_{\mathrm{L,p}}$ connected in parallel to p-th port. Tuning element at particular port is calculated as $C_p = B_{\mathrm{L},p}/\omega$ if $B_{\mathrm{L},p} > 0$ and $L_p = 1/\left(\omega B_{\mathrm{L},p}\right)$ in the opposite case.

The previous equations are used to convert a bilinear form $\mathbf{I}^{\mathrm{H}}\mathbf{MI}$ to its port-mode equivalent as

$$\mathbf{I}^{\mathrm{H}}\mathbf{MI} = \mathbf{v}^{\mathrm{H}}\mathbf{mv}, \tag{2.26}$$

where $\mathbf{m} = \mathbf{P}^{\mathrm{H}}\mathbf{D}^{\mathrm{H}}\mathbf{Y}^{\mathrm{H}}\mathbf{MYDP}$. When $\mathbf{M} = \mathbf{Z}$ with $\mathbf{Z}$ being expressed by its radiation, losses and reactance parts, expression for complex power is rewritten as

$$\mathbf{I}^{\mathrm{H}}\mathbf{ZI} = \mathbf{v}^{\mathrm{H}}\mathbf{y}^{\mathrm{H}}\mathbf{v} = \mathbf{v}^{\mathrm{H}}\left(\mathbf{g}_0 + \mathbf{g}_\rho - \mathrm{i}\mathbf{b}_0\right)^{\mathrm{H}}\mathbf{v}, \tag{2.27}$$

where $\mathbf{g}_0$, $\mathbf{g}_\rho$, and $\mathbf{b}_0$ represent port mode representation of $\mathbf{R}_0$, $\mathbf{R}_\rho$, and $\mathbf{X}_0$ matrices respectively[3]. Port-mode representation of far-field vector $\mathbf{f}$ is obtained in a similar manner as

$$\mathbf{f}\left(\hat{\boldsymbol{r}}, \hat{\boldsymbol{e}}\right) = \mathbf{F}\left(\hat{\boldsymbol{r}}, \hat{\boldsymbol{e}}\right)\mathbf{YDP}. \tag{2.28}$$

[2] Considering RWG basis functions [25], ζ_m is equal to the edge length l_m of the corresponding basis function $\boldsymbol{\psi}_m\left(\boldsymbol{r}\right)$.

[3] Be aware of change of units from Ohms to Siemens.

The quantities defined above allow to express antenna figures of merit in port-mode basis. The input power $P_{\text{in}} = \mathbf{a}^{\text{H}}\mathbf{a}/2$ and radiated power expressed from (2.27) are used to evaluate total active reflection coefficient Γ^{t} as [19]

$$\Gamma^{\text{t}} = \sqrt{1 - \frac{\mathbf{v}^{\text{H}}\mathbf{g}_0\mathbf{v}}{\mathbf{v}^{\text{H}}\mathbf{k}_{\text{i}}^{\text{H}}\mathbf{k}_{\text{i}}\mathbf{v}}}, \tag{2.29}$$

where $\mathbf{a}$ is expressed via (2.24). Total efficiency is evaluated directly from (2.29) as

$$\eta_{\text{tot}} = \frac{\mathbf{v}^{\text{H}}\mathbf{g}_0\mathbf{v}}{\mathbf{v}^{\text{H}}\mathbf{k}_{\text{i}}^{\text{H}}\mathbf{k}_{\text{i}}\mathbf{v}}, \tag{2.30}$$

and radiation efficiency expressed in port-mode terms reads

$$\eta_{\text{rad}} = \frac{1}{1+\delta}, \tag{2.31}$$

with $\delta = \mathbf{v}^{\text{H}}\mathbf{g}_\rho\mathbf{v}/(\mathbf{v}^{\text{H}}\mathbf{g}_0\mathbf{v})$ being dissipation factor. Q-factor is converted to[4]

$$Q = \frac{1}{2}\frac{\mathbf{v}^{\text{H}}\mathbf{w}\mathbf{v}}{\mathbf{v}^{\text{H}}\mathbf{g}_0\mathbf{v}} + \frac{1}{2}\frac{\left|\mathbf{v}^{\text{H}}\mathbf{b}_0\mathbf{v}\right|}{\mathbf{v}^{\text{H}}\mathbf{g}_0\mathbf{v}}. \tag{2.32}$$

Finally, realized gain reads

$$G^{\text{t}} = \frac{4\pi}{Z_0}\frac{\mathbf{v}^{\text{H}}\mathbf{f}^{\text{H}}\mathbf{f}\mathbf{v}}{\mathbf{v}^{\text{H}}\mathbf{k}_{\text{i}}^{\text{H}}\mathbf{k}_{\text{i}}\mathbf{v}}, \tag{2.33}$$

which was obtained from product of (2.30) with (2.13), expressed in port-mode quantities.

[4] The second part represents tuning element Q-factor, ideal capacitors and inductors connected in parallel to port are assumed.

Chapter 3

Optimization

Optimization problems for maximization of total efficiency, and therefore minimization of total active reflection coefficient, are stated in this chapter. Their solution is demonstrated in cases of 1-port and 2-port antennas. Relations valid for the latter one can be generalized for a p-port antenna. Section 3.3 also shows a comparison of both discussed cases. The last section shows a relation of total active coefficient to Q-factor and fractional bandwidth.

3.1 Formulation of Optimization Problems

The optimization process is separated into combinatorial optimization [26] of ports placement, and into nonlinear optimization of impedance matching operating over convex optimization [27] of feeding voltages.

The port placement optimization consists of an exhaustive search of the best result obtained from the other part of the optimization process. Considering p-port antenna with n possible positions, there is in total $n!/p!(n-p)!$ possible combinations of particular ports. It is worth saying that this number can be significantly reduced by taking into account unique solutions only (*i.e.*, omitting symmetrical placements).

Considering one particular fixed combination of ports, the optimization process is further divided into two coupled parts.

1. Finding optimal terminating impedances, which depend on feeding voltages.

2. Finding optimal feeding voltages with convex optimization, which are, however dependent on terminating impedance.

This coupling between the two subproblems results in nonlinear behavior. It, nevertheless, will be shown that in some favorable cases both problems can be separated.

Optimization problem for the maximal total efficiency reads [19]

$$\begin{aligned} \underset{\mathbf{v},\mathbf{\Lambda},\mathbf{y}_\mathrm{L}}{\text{maximize}} \quad & \mathbf{v}^\mathrm{H}\mathbf{g}_0\mathbf{v} \\ \text{subject to} \quad & \mathbf{v}^\mathrm{H}\mathbf{k}_\mathrm{i}^\mathrm{H}\mathbf{k}_\mathrm{i}\mathbf{v} = 1, \end{aligned} \tag{3.1}$$

which, considering fixed impedances $\mathbf{\Lambda}$ and tuning susceptance elements $\mathbf{y}_\mathrm{L}$ in (2.24), is solved via generalized eigenvalue problem (GEP)

$$\mathbf{g}_0\mathbf{v}_n = \eta_n \mathbf{k}_\mathrm{i}^\mathrm{H}\mathbf{k}_\mathrm{i}\mathbf{v}_n, \tag{3.2}$$

where the largest eigenvalue η_1 and corresponding eigenvector $\mathbf{v}_1$ form the solution to (3.1). Analogous optimization problem applies to the optimal radiation efficiency [19]

$$\begin{aligned} \underset{\mathbf{v}}{\text{minimize}} \quad & \mathbf{v}^\mathrm{H}\mathbf{g}_\rho\mathbf{v} \\ \text{subject to} \quad & \mathbf{v}^\mathrm{H}\mathbf{g}_0\mathbf{v} = 1, \end{aligned} \tag{3.3}$$

with solution obtained as the smallest eigenvalue and corresponding eigenvector of

$$\mathbf{g}_\rho\mathbf{v}_n = \delta_n \mathbf{g}_0\mathbf{v}_n, \tag{3.4}$$

with δ_1 being dissipation factor resulting in the best possible radiation efficiency. Unlike the previous problem, optimization task (3.3) is not dependent on matching network.

Matching efficiency is maximized if reflections are zeroed. This is equivalent to problem

$$\begin{aligned} \underset{\mathbf{v},\mathbf{\Lambda},\mathbf{y}_\mathrm{L}}{\text{minimize}} \quad & \mathbf{v}^\mathrm{H}\mathbf{k}_\mathrm{r}^\mathrm{H}\mathbf{k}_\mathrm{r}\mathbf{v} \\ \text{subject to} \quad & \mathbf{v}^\mathrm{H}\mathbf{k}_\mathrm{i}^\mathrm{H}\mathbf{k}_\mathrm{i}\mathbf{v} = 1. \end{aligned} \tag{3.5}$$

Considering fixed voltages $\mathbf{v}$, problem (3.5) leads to nonlinear optimization and has multiple solutions leading to zero reflected power. Although this might be seen as a complication, it is shown in latter that this non-uniqueness brings a possibility of an analytical solution to the problem.

Optimization problems (3.1)–(3.5) are now solved and described further for the case of 1-port and 2-port antennas in the rest of this chapter.

3.2 Optimization of 1-port Antenna

Considering a 1-port antenna, all port matrices reduce to scalars, *e.g.*, $\mathbf{a} \to a$. It is also easy to verify that metrics (2.29)–(2.33) are all independent of a particular feeding scenario in this case[1]. Antenna performance here only depends on the position of a single port, on corresponding tuning element B_L and, finally, on the impedance of connected transmission line R_c. Due to the symmetry of the problem and the selected discretization, only 22 feeding positions, see Figure 3.1, must be considered for ports position.

Antenna figures of merit are now studied in detail, starting with total efficiency

$$\eta_\mathrm{tot} = \frac{g_0}{|k_\mathrm{i}|^2}, \tag{3.6}$$

[1] Feeding voltage amplitude is nonzero of course.

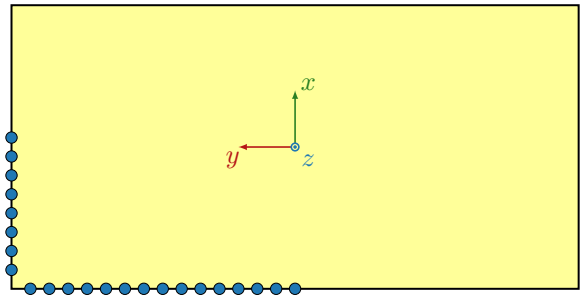

Figure 3.1: Places considered for port positions of 1-port antenna. Each position is depicted by a blue circular marker.

where incident wave matrix, now reduced to a scalar, reads

$$k_\mathrm{i} = \frac{1}{2\sqrt{R_\mathrm{c}}}\left(1 + R_\mathrm{c}\left(y + y_\mathrm{L}\right)\right), \tag{3.7}$$

with $y = g_0 + g_\rho - \mathrm{i}b_0$ and $y_\mathrm{L} = \mathrm{i}B_\mathrm{L}$. The reflected wave matrix reads

$$k_\mathrm{r} = \frac{1}{2\sqrt{R_\mathrm{c}}}\left(1 - R_\mathrm{c}\left(y + y_\mathrm{L}\right)\right), \tag{3.8}$$

and can be used to perform impedance matching. Setting (3.8) equal to zero results in

$$y = \frac{1}{R_\mathrm{c}} - \mathrm{i}B_\mathrm{L}, \tag{3.9}$$

which after separation into real and imaginary part reads

$$g_0 + g_\rho = \frac{1}{R_\mathrm{c}}, \tag{3.10}$$

$$b_0 = B_\mathrm{L}, \tag{3.11}$$

giving the necessary impedance R_c and susceptance B_L. Using (3.10) and (3.11) in (3.6) results in maximal achievable efficiency, ensuring zero reflected power.

With the values of B_L and R_c being fixed, other metrics depend only on the position of a feeding port. The radiation efficiency reads

$$\eta_\mathrm{rad} = \frac{g_0}{g_0 + g_\rho}, \tag{3.12}$$

Q-factor is simplified to

$$Q = \frac{1}{2}\frac{w + |b_0|}{g_0}, \tag{3.13}$$

with $b_0 = B_\mathrm{L}$ being the susceptance of the tuning element, see (3.11). Finally, the realized gain[2] reads

$$G_\mathrm{t} = \frac{4\pi}{Z_0}\left|\frac{f\left(\hat{\boldsymbol{r}}, \hat{\boldsymbol{e}}\right)}{k_\mathrm{i}}\right|^2. \tag{3.14}$$

[2]Realized gain is evaluated as sum of $\hat{\boldsymbol{\theta}}$ and $\hat{\boldsymbol{\varphi}}$ polarizations at the direction $\theta = 180°$ and $\varphi = 0°$.

Resulting optimized total active reflection coefficient Γ^{t} is shown in Figure 3.2 together with magnitude of the reflection coefficient Γ. It can be seen that Γ^{t} is more stricter than Γ and that bandwidth evaluated from Γ^{t} is slightly lower than the one evaluated from Γ. Total active reflection coefficient obtained from CST [12] is based on same matching as the Γ^{t} evaluated with AToM [11]. Shift in frequency is a consequence of discrepancies in input admittance, see Appendix B.2.

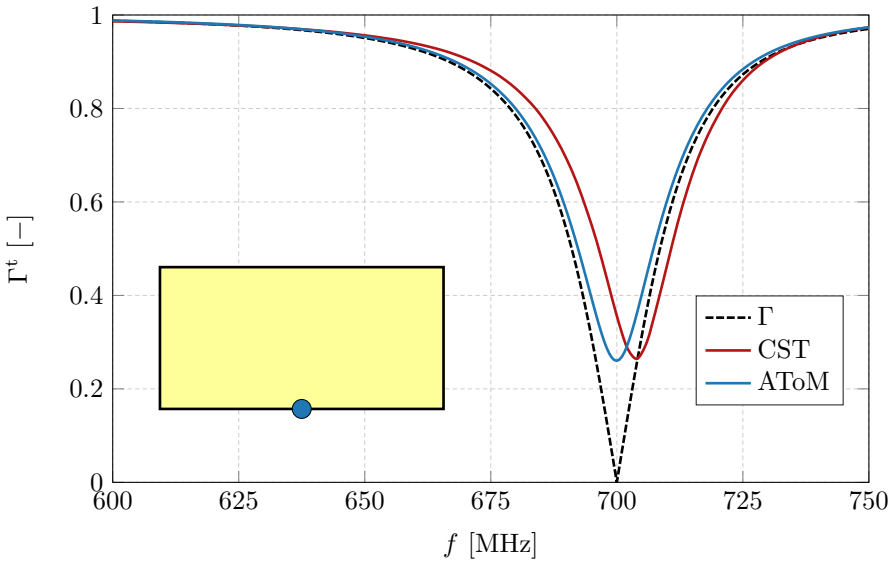

Figure 3.2: Optimal total active reflection coefficient Γ^{t} for 1-port antenna designed at frequency 700 MHz. Inset show optimal position of antenna port. Black dashed line depicts reflection coefficient Γ. Antenna is made of copper.

Table 3.1 shows results of selected figures of merit with total active reflection coefficient minimized at frequency 700 MHz. The antenna is tuned to resonance with the parallel capacitor of capacitance C.

3.3 Optimization of 2-port Antenna

Multi-port antennas are far more challenging than 1-port antennas. Incorrect port feeding[3] may result in undesired interference.

Considering 2-port antenna, the analytical description is still possible. Antenna metrics stated in Section 2.2 are in the form

$$\xi(\mathbf{v}) = \frac{\mathbf{v}^{\mathrm{H}}\mathbf{a}\mathbf{v}}{\mathbf{v}^{\mathrm{H}}\mathbf{b}\mathbf{v}}, \tag{3.15}$$

where ξ represents particular metric and $\mathbf{a}$ and $\mathbf{b}$ are general Hermitian matrices. In case of 2-port antennas, relation (3.15) can be simplified to

$$\xi(\mathbf{v}) = \frac{a_{11} + 2\nu\left(\mathrm{Re}\{a_{12}\}\cos\phi - \mathrm{Im}\{a_{12}\}\sin\phi\right) + \nu^2 a_{22}}{b_{11} + 2\nu\left(\mathrm{Re}\{b_{12}\}\cos\phi - \mathrm{Im}\{b_{12}\}\sin\phi\right) + \nu^2 b_{22}}. \tag{3.16}$$

[3] Such amplitudes and phases of feeding voltages that excite self-canceling port modes in (2.22).

Two complex variables (v_1, v_2) in (3.16) are reduced to two real variables, $\nu = |v_2| / |v_1|$, and $\phi = \arg v_1 - \arg v_2$. If $\nu \to 0$, feeding is reduced to the first port, and with $\nu \to \infty$ only second port is used. The conditions $\nu > 0$ and $\phi \in [0, \pi]$ are considered to further reduce the solution space. Interesting case occurs for symmetrical position of both ports, when all stated matrix operators above are real symmetric matrices. Formula (3.16) then reduces to

$$\xi(\mathbf{v}) = \frac{(1+\nu^2)\, a_{11} + 2\nu a_{12} \cos\phi}{(1+\nu^2)\, b_{11} + 2\nu b_{12} \cos\phi}. \tag{3.17}$$

Differentiating (3.17) with respect to ν and ϕ leads to set of equations with two stationary points, $(\nu, \phi) = (1, 0)$ and $(\nu, \phi) = (1, \pi)$, which if substituted back to (3.17) gives

$$\xi(1,0) = \frac{a_{11} + a_{12}}{b_{11} + b_{12}}, \quad \text{and} \quad \xi(1,\pi) = \frac{a_{11} - a_{12}}{b_{11} - b_{12}}. \tag{3.18}$$

The solution to the original problem of maximization of (3.15) is then the higher one from solutions in (3.18). One another interesting case is when $a_{11}/a_{12} = b_{11}/b_{12}$. If this condition is fulfilled, the figure of merit ξ is independent of the feeding scheme[4].

It is convenient for minimization of total active reflection coefficient if antenna is in resonant state

$$\mathbf{v}^{\mathrm{H}} \mathbf{b}_0 \mathbf{v} = 0. \tag{3.19}$$

Considering connecting parallel tuning susceptances to each port, modified resonant condition reads

$$\mathbf{v}^{\mathrm{H}} (\mathbf{b}_0 + \mathbf{b}_{\mathrm{L}})\, \mathbf{v} = 0. \tag{3.20}$$

If feeding voltages $\mathbf{v}$ are fixed, condition (3.20) can be solved as

$$(\mathbf{b}_0 + \mathbf{b}_{\mathrm{L}})\, \mathbf{v} = \mathbf{0}, \tag{3.21}$$

where tuning susceptance at m-th port can be always found as

$$b_{\mathrm{L},m} = -\sum_{n=1}^{P} b_{0,mn} \frac{v_n}{v_m}, \tag{3.22}$$

and therefore fulfilling (3.20).

Considering applied tuning (3.22), incoming and reflected power waves read

$$\mathbf{a} = \frac{1}{2} (\mathbf{E} + \mathbf{\Lambda} (\mathbf{g}_0 + \mathbf{g}_\rho)\, \mathbf{\Lambda})\, \mathbf{\Lambda}^{-1} \mathbf{v}, \tag{3.23}$$

$$\mathbf{b} = \frac{1}{2} (\mathbf{E} - \mathbf{\Lambda} (\mathbf{g}_0 + \mathbf{g}_\rho)\, \mathbf{\Lambda})\, \mathbf{\Lambda}^{-1} \mathbf{v}, \tag{3.24}$$

[4] This could happen for two parallel dipoles of specific length and spacing.

because imaginary parts of incoming voltage wave (2.24) and reflected voltage wave (2.25) are zeroed. Optimal impedance $R_{c,m}$ of m-th feeding line is therefore evaluated as

$$R_{c,m} = \left(\sum_{n=1}^{P} g_{mn} \frac{v_n}{v_m} \right)^{-1}, \tag{3.25}$$

where $g_{mn} = g_{0,mn} + g_{\rho,mn}$. Fulfilling conditions (3.22) and (3.25) will ensure zero reflected power and thus perfect matching efficiency. Relations (3.22) and (3.25) require real feeding voltages, which, however, is always ensured by generalized eigenvalue problems in (3.16).

The main goal of the optimization in this work is the minimization of total active reflection coefficient Γ^{t} (*i.e.* maximization of total efficiency). Considering fixed port positions, this can be done in two different ways. The first one starts with maximization of radiation efficiency η_{rad} by solving optimization problem (3.3) and continues with solution to impedance matching (3.22) and (3.25) with corresponding voltages. If the resulting impedances $R_{c,p}$ are positive, then optimal total efficiency η_{tot} equals to the optimal radiation efficiency η_{rad}[5]. If at least one of the resulting impedances $R_{c,p}$ is negative, this solution strategy cannot be used.

The other possibility is to focus directly on solving optimization problem (3.1) with optimization variables being voltages and line impedances. Optimal feeding is dependent on port termination and vice versa, which leads to nonlinear optimization. This way also leads to $\eta_{match} = 1$ and $\eta_{tot} = \eta_{rad}$, but radiation efficiency will always be equal or lower than in the previous case. Code snippet in Figure 3.3 shows MATLAB implementation of criteria function. Minimization is done with `fminsearch` function [28].

```
function minusTotEff = minimizeTARC(x)
    Rc = x(1:nP).';

    % Prevent negative line impedances
    if any(Rc < 1)
        minusTotEff = Inf;
    else
        % Modify matching impedance
        Lambda = diag(sqrt(Rc));
        ki = 1/2*(E + Lambda*(g0+gr)*Lambda) / Lambda;

        % Solve eigenvalue problem
        [vopt, totEff] = eigs(g0, ki'*ki, 1, 'la');
        minusTotEff = -real(totEff);
    end
```

Figure 3.3: Optimization problem (3.1) implementation in MATLAB .

There are in total 3655 possible combinations of port placement, which can be further reduced to 946 combinations when symmetries are applied.

[5] This would still be fulfilled even for negative line impedances, however, this work does not consider active matching elements.

Figure 3.4 depicts considered port positions. Although reduction of symmetric port positions in case of 2-port can be handled manually, it is not suitable for a higher number of considered ports, which has to be treated with utilization of point group theory [29]. However, this is beyond the scope of this work.

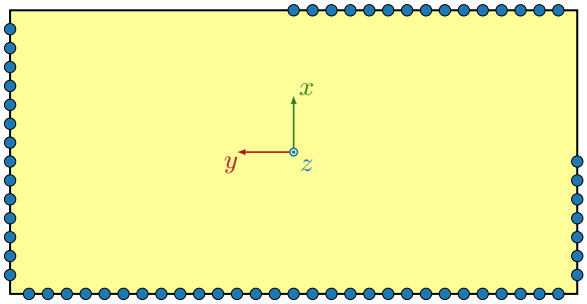

Figure 3.4: Possible positions for the feeding ports for 2-port antenna.

Figure 3.5 shows resulting optimized total active reflection coefficient. The cause of shift between curves is again shift in admittance matrices, see Appendix B.2. Port placement results in addition of symmetrically placed port to the first one and feeding voltages are uniform.

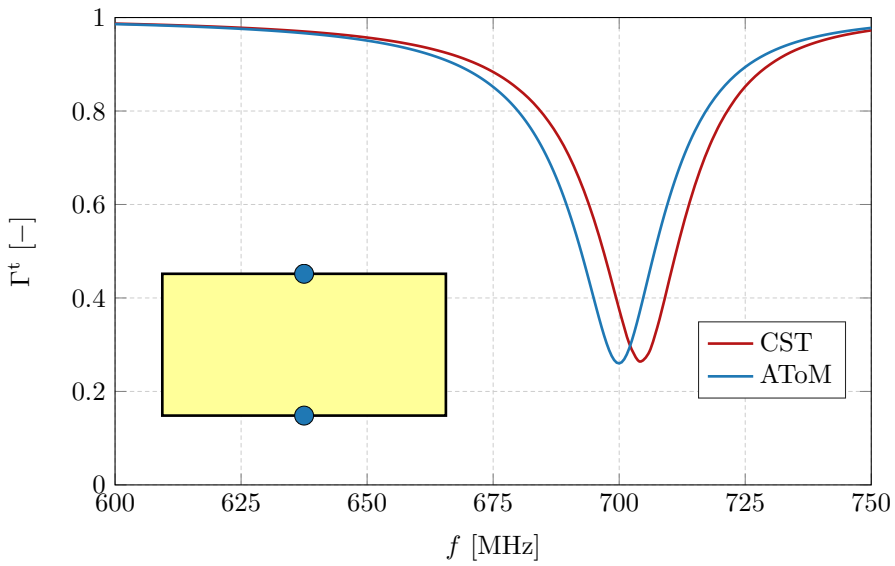

Figure 3.5: The 2-port optimized total active reflection coefficient Γ^t for frequency 700 MHz. Inset shows optimal positions of antenna ports.

Table 3.1 shows other antenna parameters obtained from the optimization.

Comparing results of this section and Section 3.2, the following conclusion is drawn. Adding another port at the same frequency seems to have no advantage over the 1-port antenna. Antenna parameters in Table 3.1 are almost equal and the total active reflection coefficient Γ^t characteristics are also almost identical, see Figure 3.6. The optimization process adds another

	R_c [Ω]	C [pF]	η_{rad} [−]	η_{tot} [−]	G^t [dBi]	Q [−]	FBW [−]
1-port	124.1	5.488	0.9323	0.9323	3.745	54.04	0.03930
2-port	62.12	11.08	0.9324	0.9324	3.751	53.97	0.03931

Table 3.1: Figures of merit for optimized 1-port and 2-port antennas at 700 MHz.

port symmetrically to the port of a 1-port antenna. Used tuning capacitors for 2-port are twice as large as for the 1-port antenna, while the characteristic impedance of the connected feeding line is two times smaller in the 2-port case than the 1-port case. This is caused by the symmetry of port placement and feeding voltages and because

$$z_{11} + z_{12} \approx \frac{z_{in}}{2}, \tag{3.26}$$

where z_{mn} are elements of impedance matrix for 2-port antenna, and z_{in} is the input impedance of the 1-port antenna.

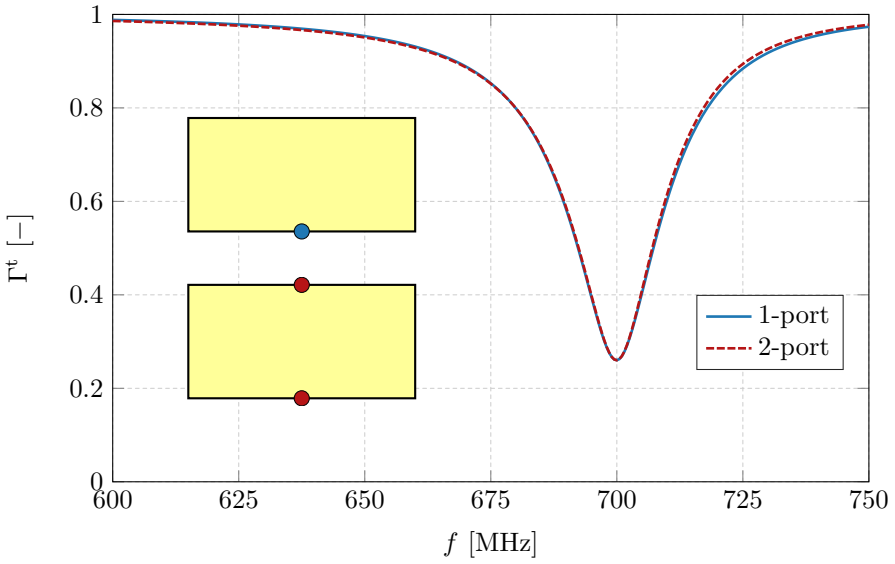

Figure 3.6: Comparison of total active reflection coefficient Γ^t performance. Insets highlight the position of ports for both antennas.

3.4 Bandwidth Performance

This work primarily focused on minimization of total active reflection coefficient, although there are several other parameters that can be the product of optimization.

There is still one unresolved hypothesis.

- Is there any relation between Q-factor and fractional bandwidth evaluated from total active reflection coefficient?

The total active reflection coefficient Γ^{t} and Q-factor were evaluated for all possible combinations of port placement of the 2-port antenna and their trade-off is plotted, with respect to ascending sorting of Γ^{t}, in Figure 3.7. Relation (2.8) is now rewritten to obtain equivalent Q-factor evaluated from fractional bandwidth

$$Q_{\mathrm{FBW}} = \frac{2\sqrt{\beta}}{\mathrm{FBW}}, \tag{3.27}$$

with $\sqrt{\beta} = 1$ being proportionality constant [18]. Both resulting curves are showing high correlation with each other and, quite surprisingly, total active reflection coefficient is increasing with increasing Q-factor. This implicates two following statements.

1. Radiation Q-factor represents an accurate approximation of bandwidth of multi-port antenna.

2. Minimization of total active reflection coefficient leads, in the studied setup, to maximization of bandwidth. There is not a trade-off between these parameters.

Neither of these statements can be supported or refuted by rigorous reasoning at this moment. The second statement is even in possible contradiction with [30] that showed a trade-off between radiation efficiency η_{rad} and Q-factor. However, it must be pointed out that radiation efficiency is relatively high in this work, $\eta_{\mathrm{rad}} > 0.85$, and its effect on Q-factor can be suppressed.

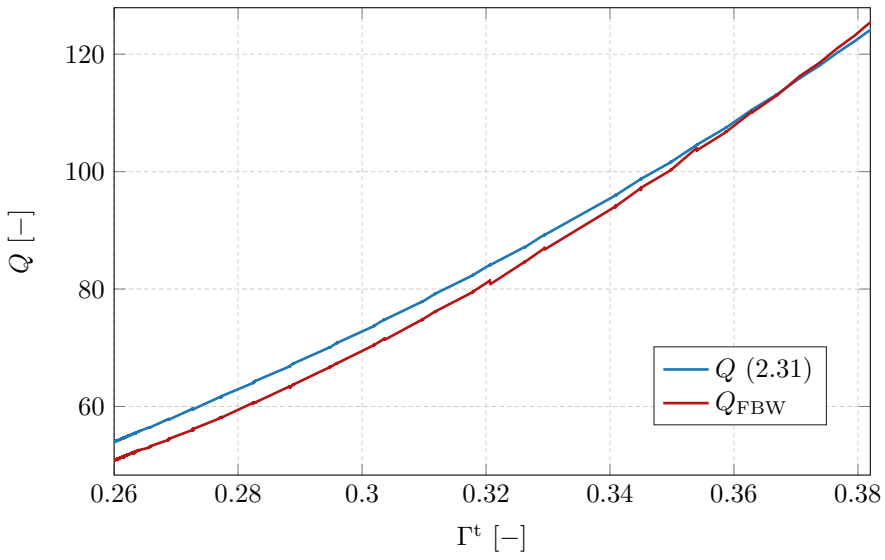

Figure 3.7: Trade-off between total active reflection coefficient Γ^{t} and Q-factor. Discrepancies at curves are caused by numerical errors highlighted by values sorting.

Chapter 4

Matching Circuits

The previous chapter assumed a simple matching network consisting of a parallel tuning element and matched transmission line. Such setup conserves the optimal feeding voltages[1], but can lead to unrealistic scenarios (*e.g.* extreme values of line impedance R_c). This chapter introduces more appropriate matching networks.

All networks introduced in this section are considered lossless[2] and consist of lumped reactances (capacitors and inductors) only, since electrical size of the used cellphone model does not allow for distributed tuning elements.

The first section introduces a method of impedance matching with network optimality criterion. The next section overviews total efficiency and its components with respect to various matching networks. The last section further discusses positioning of signal generators.

4.1 Impedance Matching Network Synthesis

An arbitrary impedance can be matched at single frequency with two reactive elements [14]. In order to capture all matching possibilities, a matching network represented by impedance matrix, see Figure 4.1,

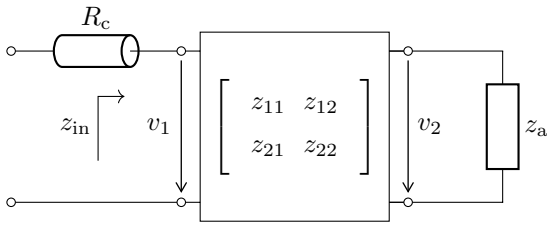

Figure 4.1: Matching network for 1-port antenna.

$$\mathbf{z}_L = \begin{bmatrix} z_{11} & z_{12} \\ z_{21} & z_{22} \end{bmatrix} = \mathrm{i} \begin{bmatrix} x_{11} & x_{12} \\ x_{21} & x_{22} \end{bmatrix}, \tag{4.1}$$

[1] Addition of parallel tuning element does not affect optimal voltages from problems (3.1)–(3.3).

[2] Lossy matching elements will further lower radiation efficiency η_{rad} and therefore total efficiency η_{tot} [31].

is used. Input impedance z_{in} on the left side of the matching network is given by v_1/i_1 and should be equal to the impedance of the feeding line, therefore

$$z_{\text{in}} = z_{11} - \frac{z_{21}z_{12}}{z_{\text{a}} + z_{22}} = R_{\text{c}}, \tag{4.2}$$

where z_{a} is the input impedance of the standalone antenna. Separation of real and imaginary parts of (4.2) gives

$$R_{\text{c}} = \frac{r_{\text{a}}x_{21}x_{12}}{r_{\text{a}}^2 + (x_{\text{a}} + x_{22})^2}, \qquad x_{11} = \frac{(x_{\text{a}} + x_{22})\, x_{21}x_{12}}{r_{\text{a}}^2 + (x_{\text{a}} + x_{22})^2}, \tag{4.3}$$

which is a set of nonlinear equations with multiple solutions, each of them having unlimited possibilities of circuit realizations. Evaluation of normalized stored energy in the matching network

$$\omega W_{\text{L,sto}} = \frac{\omega}{2}\mathbf{i}^{\text{H}}\frac{\partial \text{Im}\left\{\mathbf{z}_{\text{L}}\right\}}{\partial\omega}\mathbf{i} = \frac{\omega}{2}\mathbf{v}^{\text{H}}\mathbf{y}_{\text{L}}^{\text{H}}\mathbf{w}_{\text{L}}\mathbf{y}_{\text{L}}\mathbf{v}, \tag{4.4}$$

where $\mathbf{i} = \mathbf{y}_{\text{L}}\mathbf{v}$, is added as an additional criterion for the selection of optimal matching network. Relation (4.4) is without further modifications valid only for L-circuit and Γ-circuit. However, any other topology is not examined with respect to stored energy in this work. Both matching networks considered here for impedance transformation are shown in Figure 4.2. Serial element X and parallel element B are either single capacitor or single inductor for which relation (4.4) applies. Matching method described above is applied

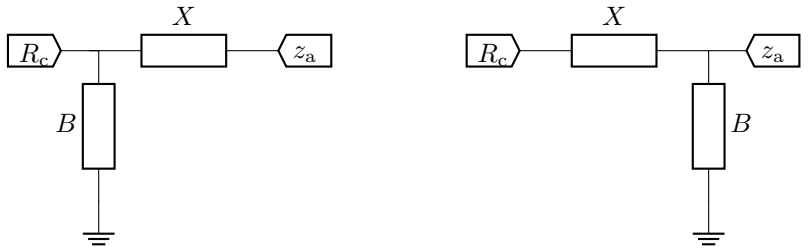

(a) : Γ-circuit. **(b) :** L-circuit.

Figure 4.2: Considered matching circuits. Ports are labeled with their impedance.

to the optimal design of the 1-port antenna, and the results are shown in Figure 4.3. Both resulting curves of total active reflection coefficient Γ^{t} are almost exactly the same showing that in this scenario, the idealized matching used in Chapter 3 can be applied for the purpose of optimization and only later, a realistic matching circuit can be synthesized with degrading the optimal performance.

In case of 2-port, optimization described in Section 3.3 returns optimal input admittances for each port p. The formulas (4.3) are then used with $z_{\text{a},p} = 1/R_{\text{c},p} - \text{i}B_{\text{L},p}$ to obtain matching circuit at p-th port. Voltages obtained from problems (3.1)–(3.5) have to be transformed to vector of generators voltages $\mathbf{v}_{\text{g}}$ due to nontrivial matching circuits as

$$\mathbf{v}_{\text{g}} = -\begin{bmatrix} y_{1,21} & 0 \\ 0 & y_{2,21} \end{bmatrix}^{-1} \left(\begin{bmatrix} y_{\text{a},11} & y_{\text{a},12} \\ y_{\text{a},21} & y_{\text{a},22} \end{bmatrix} + \begin{bmatrix} y_{1,22} & 0 \\ 0 & y_{2,22} \end{bmatrix} \right) \mathbf{v}, \tag{4.5}$$

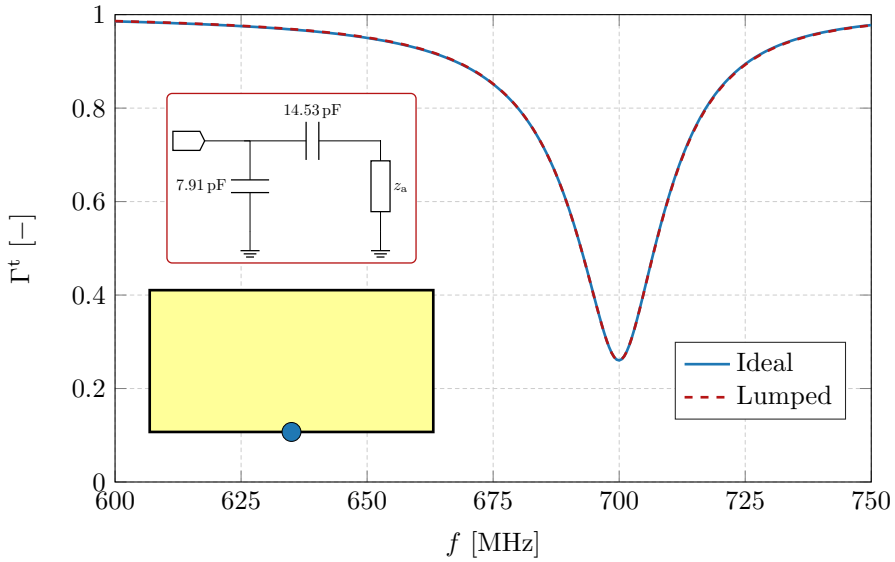

Figure 4.3: Comparison of the matching circuit consisting of parallel tuning susceptance and matched feeding line to two-element lumped element network. The first inset shows a matching circuit used for the red curve. The second inset highlights the position of feeding.

where $y_{p,mn}$ represents element of p-th port matching circuit admittance matrix, and $y_{\mathrm{a},mn}$ is element of antenna admittance matrix. Formula (4.5) is derived from cascade of two-port blocks representing matching circuits and antenna itself, see illustration in Figure 4.4.

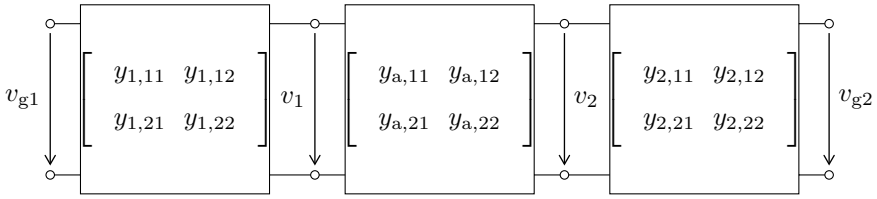

Figure 4.4: Matching network for 2-port antenna.

4.2 Effect of Matching Efficiency

The total efficiency η_{tot} is a product of matching efficiency η_{match} and radiation efficiency η_{rad}. It has been shown in the previous chapters that matching impedances maximizing η_{tot} at a particular frequency can always be found such that perfect matching is ensured and total efficiency equals radiation efficiency even for the multi-port antenna. All three efficiencies for antenna analysed in Section 3.2 are depicted in Figure 4.5. The radiation efficiency η_{rad} is almost constant in the vicinity of design frequency and is also close to its upper bound $\eta_{\mathrm{rad}}^{\mathrm{ub}}$ [31]. The bandwidth is therefore predominantly determined by matching efficiency. The gray area in Figure 4.5 represents

the upper bound to voltage standing wave ratio bandwidth [18] evaluated as

$$\mathrm{FBW}_{\mathrm{ub}}(\beta) = \frac{2\sqrt{\beta}}{Q_{\mathrm{lb}}}, \tag{4.6}$$

where Q_{lb} is the lower bound on Q-factor [32]. This suggests the existence of such feeding that would achieve better fractional bandwidth values than examined antennas above. However exciting such current will certainly lead to an excessive number of feeding ports which is highly impractical and not feasible [33]. It is therefore not addressed in this work any further.

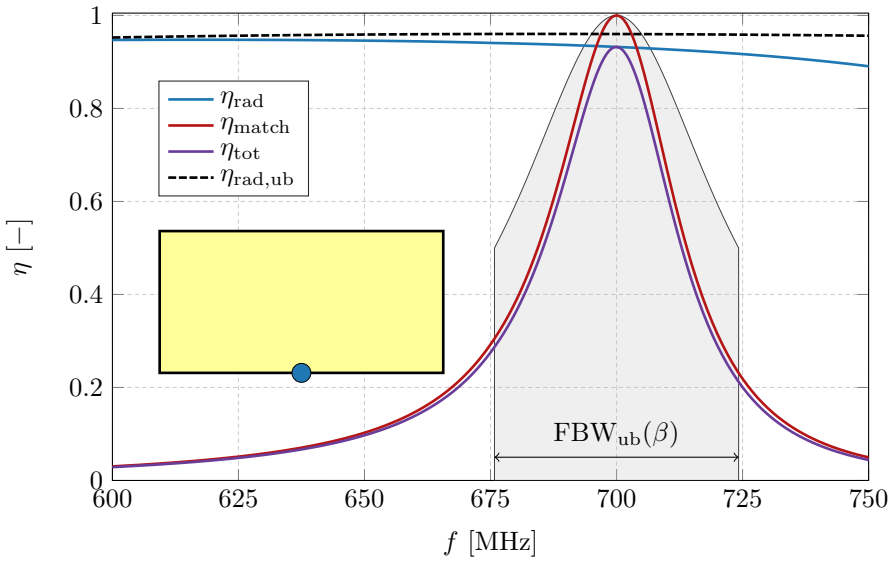

Figure 4.5: Decomposition of total efficiency into radiation efficiency and matching efficiency. Inset shows considered port position. Greyed area depicts upper bound to bandwidth. The black dashed line is the upper bound on radiation efficiency.

Cellphones requirements on matching efficiency η_{match} are not so harsh as for other radio-frequency components [34]. It is though advantageous to try to use a circuit optimized for bandwidth, which however will not ensure $\eta_{\mathrm{match}} = 1$ [14]. Figure 4.6 shows two different circuits used for impedance matching, where the second one with three lumped elements is optimized for maximal bandwidth. As is assumed, the case with the three-element matching circuit achieves higher value of total active reflection coefficient at its minimum, however, the bandwidth is wider than in the case of two-element matching circuit. One of the conclusions in Chapter 3 was that Q-factor, and therefore fractional bandwidth, and total active reflection coefficient Γ^{t} are not necessarily conflicting parameters, which seems to be in contradiction with the phenomenon observed in Figure 4.6. However, one should bear in mind the assumption of inverse proportionality between fractional bandwidth and Q-factor, that antenna is always perfectly matched to feeding [18] on design frequency. The Q-factor cannot be therefore used as an indicator of bandwidth potential in this case.

The fractional bandwidth depends on an antenna shape and on a connected matching circuit. Therefore, its maximization leads to further optimization of topology and circuit elements. However, this requires an evaluation of a large set of examined frequencies. One of the optimization possibilities is to use a set of antenna ports, each of which is tuned at a different frequency (*i.e.* achieving multi-resonant states). Another possibility are structure modifications by means of topology optimization [5, 35].

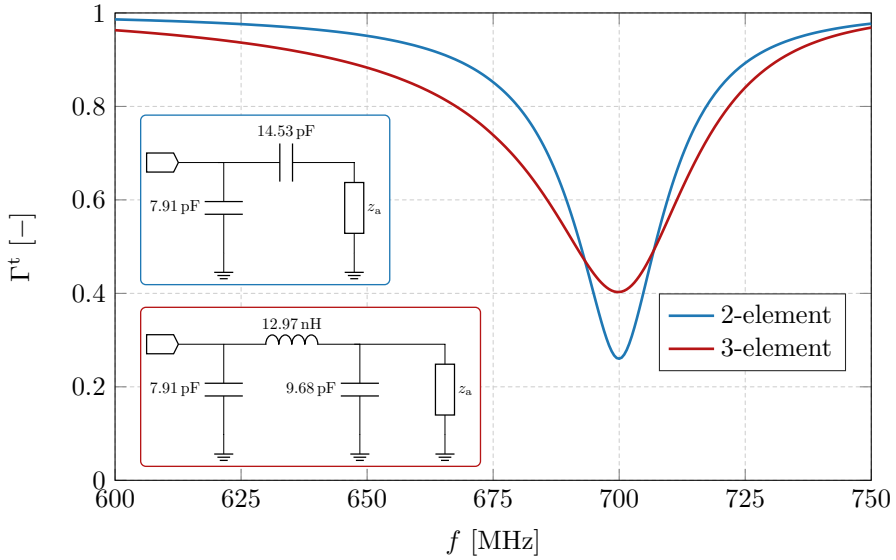

Figure 4.6: Comparison of total active reflection coefficient Γ^t for different matching circuits. Two insets show both considered circuit realizations together with their element values.

4.3 Feeding Deembedding

The position of feeding was assumed to be placed directly on the rim of the cellphone layout. However, a realistic feeding network is situated with respect to other device components. Such network can consist of fewer signal generators than there are antenna ports. Therefore, the optimal placement of the ports has to be interconnected with the matching circuitry via feeding lines. This affects stored energy (thus bandwidth performance), input impedances, and, consequently, the matching networks. The influence of the connected feeding line[3] is presented in Figure 4.7. Fractional bandwidth is lowered with the increasing length of the feeding line. This seriously questions if the proposed designs in Section 3.2 and in Section 3.3 would really be optimal in the case of some particular placement of signal generators. It also implicates the existence of another important requirement.

[3]The feeding line is physically connected to the antenna rim. It is included in the full-wave evaluation of impedance matrix.

- Considering given positions of antenna ports on the rim and given positions of matching circuitry, there is a need for simple evaluation of feeding line effect on antenna performance without change of geometry and therefore reevaluation of impedance matrix **Z**.

Without it, the computational time required to investigate all possible placements of the ports would be immense.

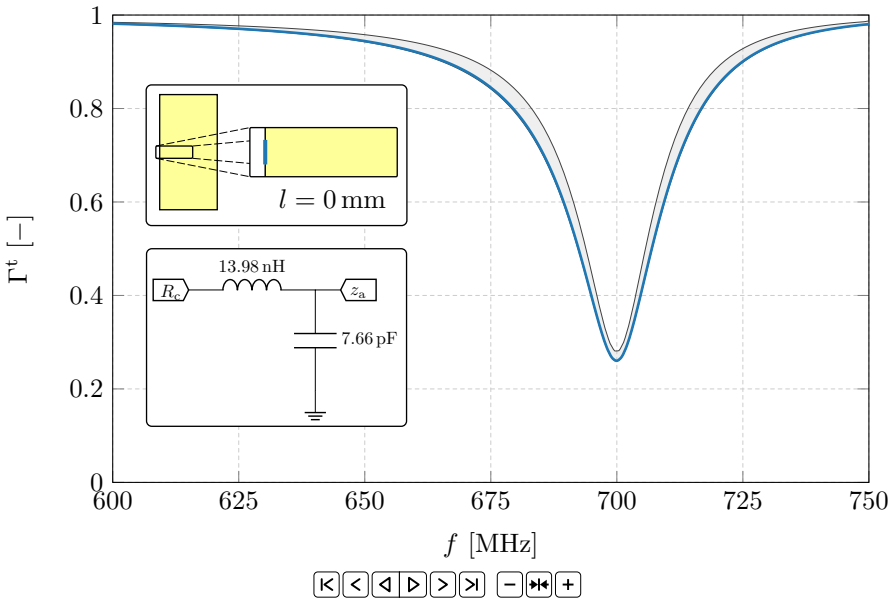

Figure 4.7: The effect of increasing length of a feeding line on resulting total active reflection coefficient Γ^t. The upper inset shows shift of port position l from the rim. The lower inset shows variations in matching circuit elements. The greyed area highlights the region spanned by all depicted shifts. To run the animation, open the document in a suitable PDF viewer (*e.g.* Adobe Acrobat Reader).

The 2-port antenna studied in the Section 3.3 is now considered with both ports connected to the feeding lines, which are heading to one voltage generator placed in the center of the ground plane[4]. There are two possible ways how to deal with matching circuits[5].

1. Each antenna port has its own matching circuit, which are then connected to the splitter, see Figure 4.8.

2. Antenna ports are connected to the splitter, which is matched to generator impedance, see Figure 4.9.

[4]The optimal solution from Section 3.3 still applies since it is least affected by length of the feeding line which is the shortest possible.

[5]The uniform feeding voltages resulting from optimization are assumed. The phase-shifters and more complicated splitters would have to be used otherwise.

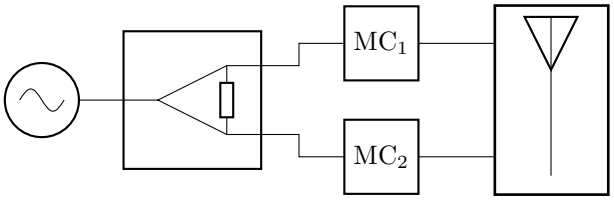

Figure 4.8: The 2-port antenna matched with two matching circuits.

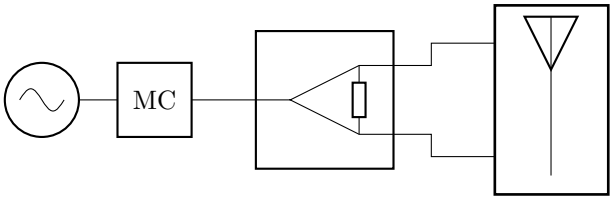

Figure 4.9: The 2-port antenna matched with one matching circuit.

Those two options were analyzed, and the resulting total active reflection coefficient Γ^{t} is shown in Figure 4.10. It can be seen that, for the considered scenario, a case with two matching circuits is only negligibly better than a case with only one matching circuit. It is, therefore, more advantageous to work further only with the antenna with one shared matching circuit. Figure 4.10 also depicts significant effect of connected feeding line as in previous case of the 1-port antenna in Figure 4.7.

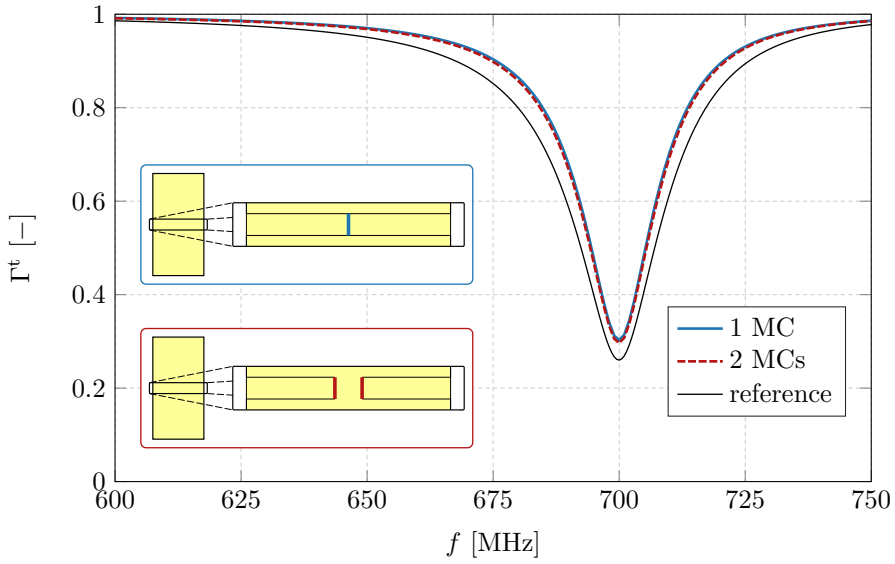

Figure 4.10: Comparison of 2-port antenna with one or two matching circuits. Black line represents resulting 2-port antenna from Section 3.3. Two insets indicates positions of matching circuits. Blue and red lines in pictures indicate positions of ports

The placement and number of used signal generators will further affect the whole optimization process. This brings another constraint/degree of freedom

to be considered. The number and placement of signal generators is fixed to the one generator placed to the center of the ground plane in this work. Other positions are not considered.

Chapter 5

Manufactured and Measured Prototype

This chapter describes necessary adjustments to the studied radiator and the matching circuits that allows for building a feasible prototype. Comparison of simulation results with measurement is presented later in Section 5.2.

5.1 Prototype Description

The model studied above in Chapter 3 and Chapter 4 was made as simple as possible to allow for the fast optimization process. However, such model is not directly realizable and has to be adjusted to ensure physical realization. Those changes will alter the electromagnetic behavior of the whole model. The realized design is based on the 1-port antenna discussed in Section 3.2. Conclusion in Section 3.3 claims that designs of 1-port antenna and 2-port antenna are equal in this particular case. Therefore the 2-port antenna is not addressed here because of additional complexity and because of economic burden.

More realistic model is shown in Figure 5.1. The changes to the original setup are:

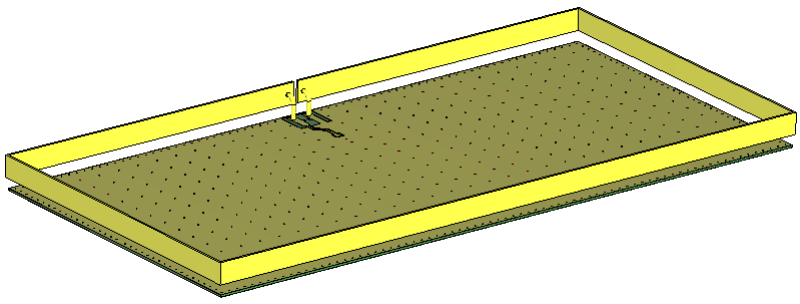

Figure 5.1: Realistic cellphone model used for simulations.

1. A realistic metallization of finite thickness is assumed both for the ground plane and the rim.
   a. The rim is made of high-quality copper sheets with thickness 0.5 mm. Because of a problem with the supplier, rim height has been changed

just before fabrication to 5 mm, see Figure 1.1. However, these changes were incorporated back into the model, and the optimization was repeated, leading to new values of matching circuitry.

b. Material selected for ground plane is IS400 [36]. It contains via holes to reduce wave guidance between the metallic plates. Dimensions of this material are depicted in Figure 5.2

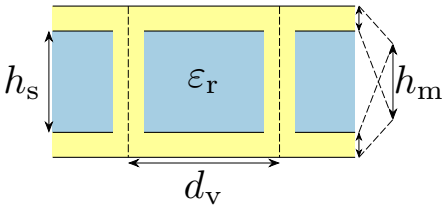

Figure 5.2: Description of ground plane material (side view). Dimensions are not in correct scale to each other. Both metal plates have height $h_m = 35\,\mu m$. Dielectric has height $h_s = 0.5\,mm$ and dielectric constant $\varepsilon_r = 3.9$. Distance between centers of via holes is $d_v = 2\,mm$ at the edge of plate and $d_v = 5\,mm$ inside.

The total height of the model has increased from 4.5 mm to 7.82 mm.

2. Antenna feeding and matching consists of several parts, see Figure 5.3. A coaxial connector is mounted at place ①. The inner conductor is connected to the patch in place ① and the outer conductor is connected to the surrounding ground. The feeding network is connected to the ground plane at position ②. This connection is used for impedance symmetrization and results in additional dips in reflection coefficient as can be seen from Figure 5.4. Tuning capacitor is connected between positions ③ and ④. The selected capacitor is of MLCC type with capacity $C = 6\,pF$ and has low loss [37].

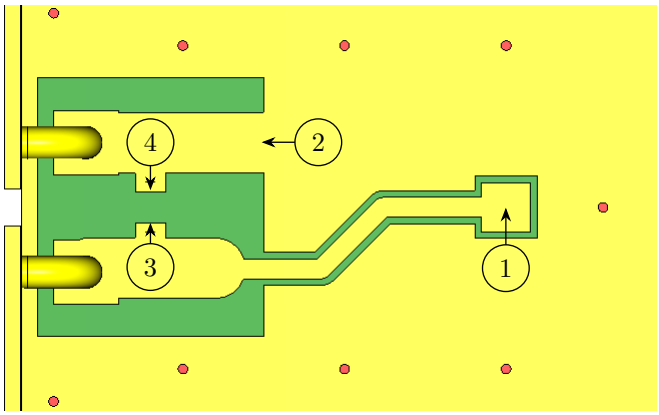

Figure 5.3: Description of antenna feeding network. Numbers in circles highlight particular places that are referred to.

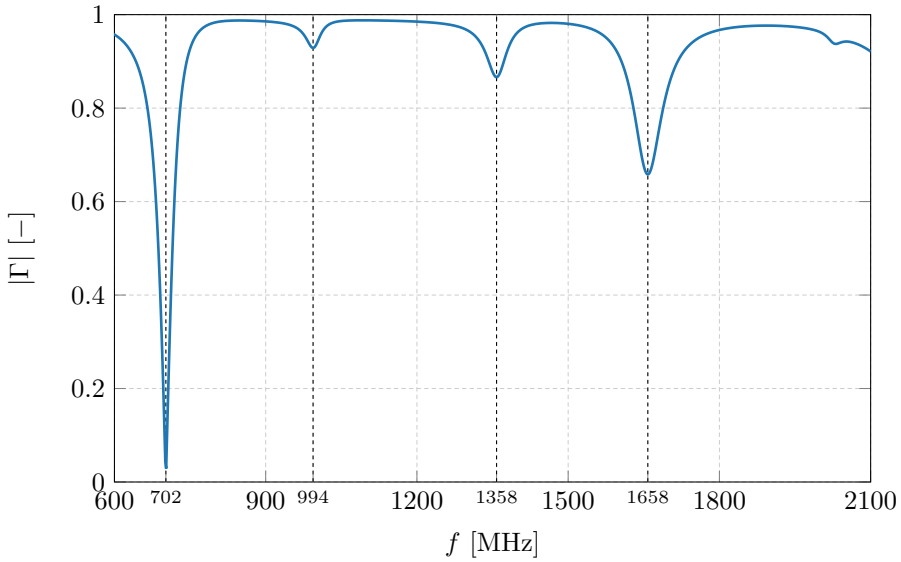

Figure 5.4: Wide-band frequency sweep of reflection coefficient Γ of a realistic simulation model. Black dashed lines highlight local minima of reflection coefficient.

3. Rim is supported by polystyrene blocks lying on ground plane. The material used has its relative permittivity close to unity and its electromagnetic interaction can be neglected.

5.2 Measurement

Physical realization of the antenna prototype is shown in Figure 5.5. The

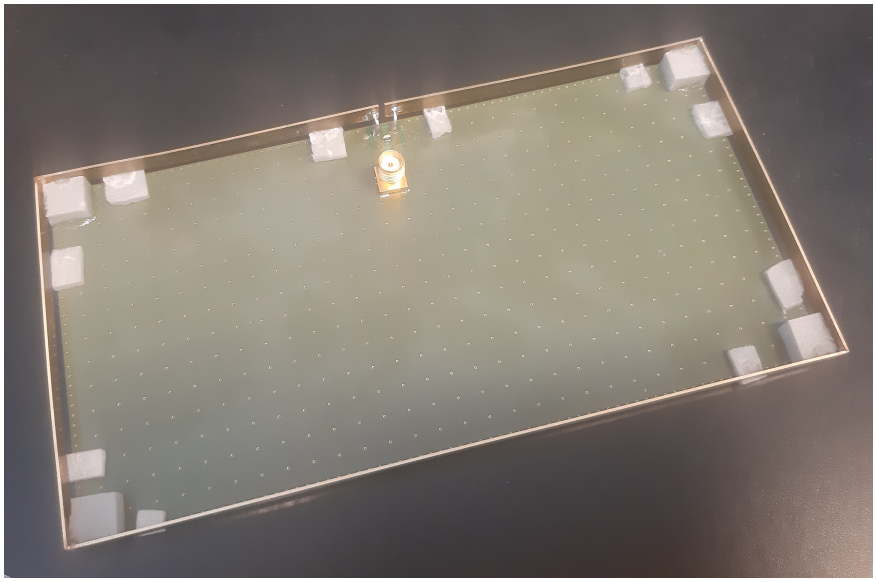

Figure 5.5: Photography of realized antenna.

prototype was using the facility available at the Department of Electromagnetic Field at Czech Technical University. All measurements were done with vector network analyser Rohde & Schwartz ZVA 40 [38]. Measurement setup in anechoic chamber is shown in Figure 5.6. Magnitude of measured reflection

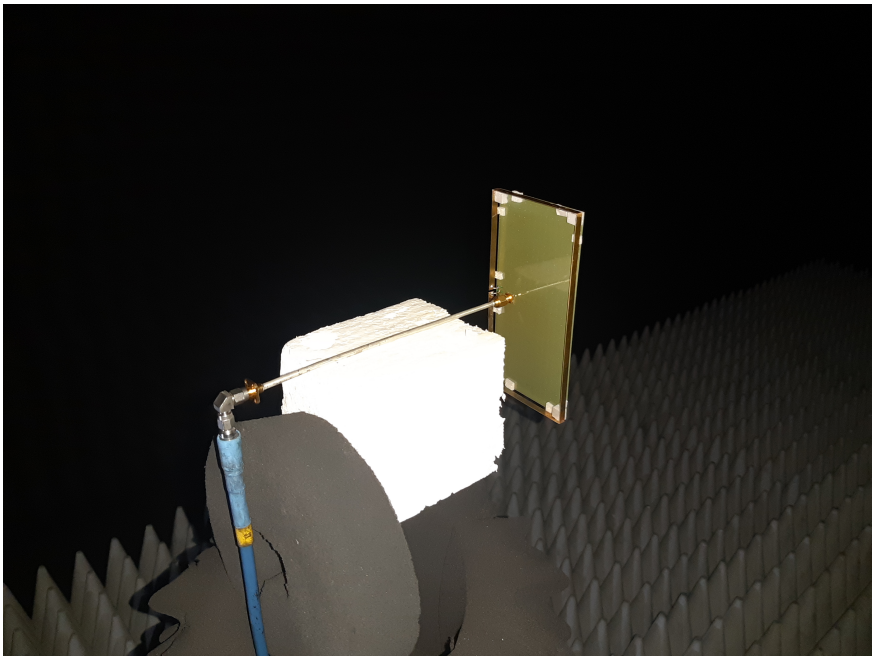

Figure 5.6: Photography of the antenna in the anechoic chamber. A low permittivity polystyrene block is used to support the antenna at the turntable which is covered by absorbing material.

coefficient is shown in Figure 5.7 and selected parameters are pointed out in Table 5.1. The measurement is compared to simulation model described in Section 5.1 and to the modified simple model used in Chapter 3 and Chapter 4. Simulation models have a great agreement with each other. The measured model uses capacitance resulting from the model described above. The frequency shift occurs between simulation and measurements. It might be reduced with different tuning capacitor. However, the same values of tuning elements are intentionally used so we are able to observe conformity of the simulation model with its physical realization.

	AToM	CST	Measurement
f_c [MHz]	700	703	723
C [pF]	5.80	6.0	6.0
FBW [−]	0.064	0.070	0.069

Table 5.1: Comparison of simulation models with measurement. Symbol f_c represents center frequency.

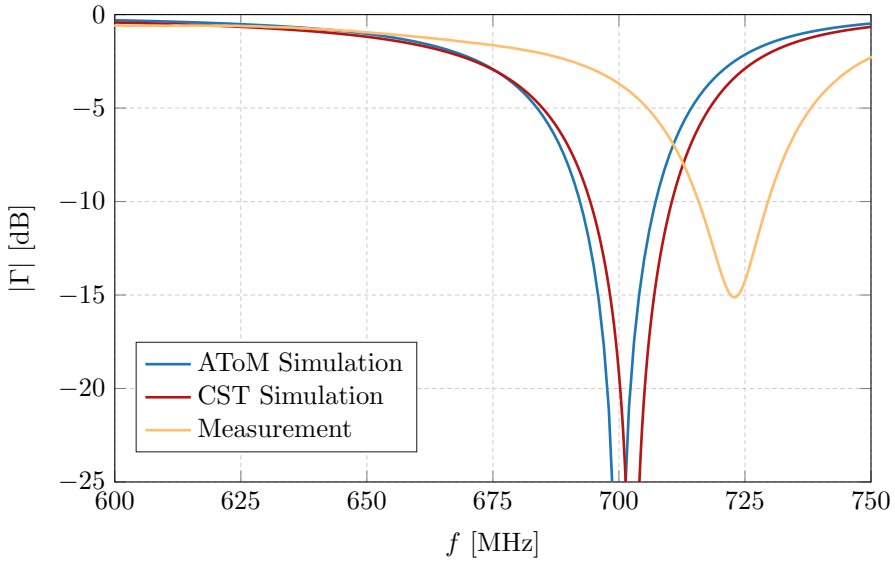

Figure 5.7: Comparison of a magnitude of the reflection coefficient for simulated and measured antennas.

Measured radiation patterns are shown in Figure 5.8 and Figure 5.9. Comparing the measured and simulated radiation patterns, it can be seen that both cuts have good conformity in direction $\theta = 180°$. The opposite direction is disturbed due to the presence of an absorber, which was used to suppress the effect of the feeding cable, see Figure 5.6.

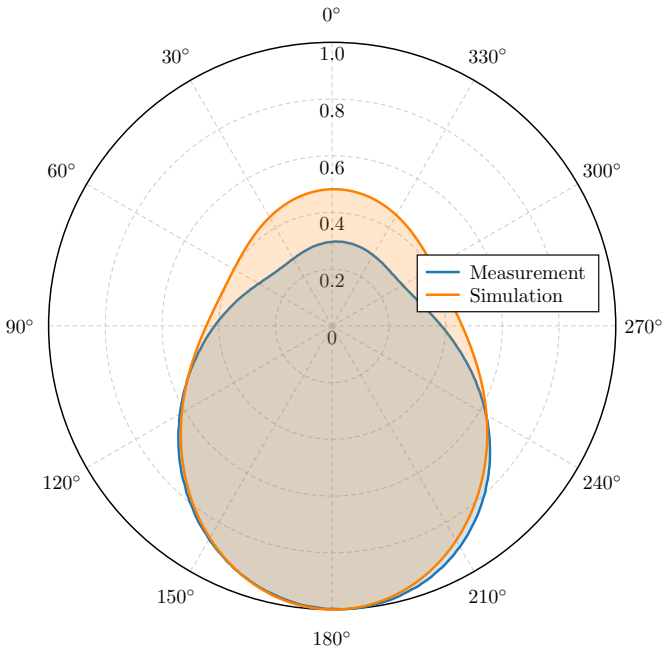

Figure 5.8: Comparison of measured and simulated radiation patterns. Vertical polarization ($\varphi = 0°$) was used.

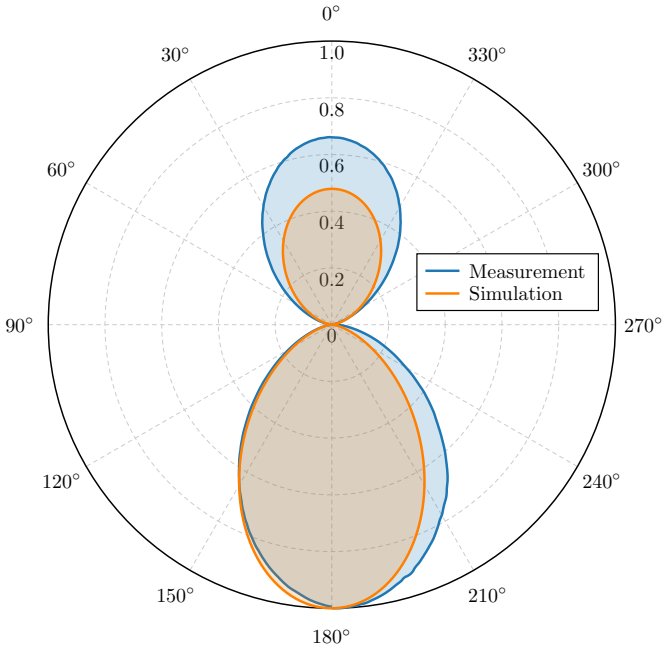

Figure 5.9: Comparison of measured and simulated radiation pattern for horizontal polarization ($\varphi = 90°$).

Radiation efficiency is not shown here because of the problem which occurred in chosen methodology. Measurement of this parameter is in general complicated [39, 40] and will be addressed in future work.

Chapter 6

Conclusion

This work describes a simplified optimization framework for multi-port antennas. The procedure is based on a reduction of full-wave matrix operators obtained with method of moments to their port equivalents. Ohmic losses are rigorously taken into account via a Gram matrix representing the surface impedance model. All ports are assumed to be terminated with parallel tuning elements and transmission lines ensuring perfect matching. The optimal placement of the ports and the optimal excitation voltages are solved independently. The first problem is solved with exhaustive search, and the second problem is solved with convex and nonlinear optimization.

A metallic rim with parasitic ground plane is considered as the experimental model. One and two ports were considered for combinatorial optimization of their placement. For each position, the optimal voltages, optimal matching, and optimal characteristic impedance of transmission lines were found. It was shown that in terms of total active reflection coefficient minimization, considered 1-port and 2-port antennas are almost identical. The 2-port antenna only has a slight advantage in feeding line impedance which is close to $50\,\Omega$.

The optimization results were used for the construction of matching networks assembled from lumped lossless elements. The effect of this additional circuitry on the realized active reflection coefficient were shown to be negligible for the considered setup. More noticeable effect could be observed when the feeding lines are added into the antenna model.

The simulation model used for the physical realization of the prototype has a remarkable agreement with the simplified model. The manufactured antenna had to be slightly modified due to problems with the supplier. It was shown that measurement also has good conformity with simulation results. However, frequency shift was observed between design and resulting center frequency. Further manufacture of different antennas based on the results of this work is planned for the coming months.

Several statements can be made based on the results of this work:

1. Optimized total active reflection coefficient seems to not contradict with low values of Q-factor in the considered scenario, the Q-factor evaluated from port quantities still being accurate estimate of fractional bandwidth, see Figure 3.7. However, it was also shown that total active

reflection coefficient and fractional bandwidth can still be conflicting metrics since matching circuits, which do not match antenna perfectly to a given impedance, may violate assumptions of inverse fractional bandwidth proportionality to Q-factor. This leads to a difficult and still insufficiently answered question:

- Is there a way how to optimize multi-port radiators with respect to the fractional bandwidth with minimal evaluation effort?

It is desirable to have such a figure of merit because the antenna's bandwidth performance evaluated from frequency sweep is always time consuming. Optimization done in this work considers that all antenna ports share the same design frequency. However, this problem is even more complicated when ports are considered at different frequencies with the goal to realize a system operating in multiple near resonances.

2. There are in total $n!/(n-p)!p!$ combinations of ports placement for the p-port antenna with n possible positions of ports which have to be evaluated. It was shown that this number can significantly be reduced when symmetries are utilized. In the case of the 1-port and 2-port antenna, this reduction can be made manually. Considering the addition of another port (*i.e.* antenna with three ports), the total number of all combinations is $(n-2)/3$ times higher than in the case of the 2-port antenna, whereas symmetry reduction cannot be handled manually. Although the brute force approach is also possible for the low number of ports, it is not feasible for five and more ports for a sufficiently discretized rim. Future work in this direction will focus on the approach utilizing point group theory.

   The 1-port and 2-port performances are almost identical. However, it cannot be said in general what effect would have to add more ports. Figure 4.5 implicates the existence of a current $\mathbf{I}$ maximizing antenna fractional bandwidth. It is, however, questionable if this current can be excited with a reasonable amount of feeding ports. Furthermore, this is connected to the previous statement about the justification of using the relation between Q-factor and multi-port antennas fractional bandwidth.

3. The feeding network will always be placed at a different place than the antenna ports at the cellphone rim. This work solves this problem by finding optimal port positions and voltages at the antenna rim and connect them to one feeding network afterward. It was shown that this change affects fractional bandwidth and matching circuits. It would be advantageous to have this effect taken into account directly in the port optimization process. Nevertheless, even with the reduction due to port symmetries, it would take a significant amount of time to simulate each port combination with its own feeding line as the method of moment matrices will have to be repeatedly evaluated and inverted. Therefore, there is a need for a simple method, which approximates feeding lines with properly fitted two-port network blocks, and is capable of capturing

different feeding line shapes, without repeated computation and inversion of impedance matrix describing antenna. Such method is being developed currently, but it is beyond the scope of this thesis, and it is not being introduced there in more detail.

All the above-mentioned problems are closely interconnected and are the main goals of future research.

Bibliography

[1] M. Giordani, M. Polese, M. Mezzavilla, S. Rangan, and M. Zorzi, "Toward 6G Networks: Use Cases and Technologies," *IEEE Communications Magazine*, vol. 58, no. 3, pp. 55–61, 2020.

[2] B. D. Van Veen and K. M. Buckley, "Beamforming: a Versatile Approach to Spatial Filtering," *IEEE ASSP Magazine*, vol. 5, no. 2, pp. 4–24, 1988.

[3] J.-M. Hannula, T. Saarinen, A. Lehtovuori, J. Holopainen, and V. Viikari, "Tunable Eight-Element MIMO Antenna Based on the Antenna Cluster Concept," *IET Microwaves, Antennas and Propagation*, vol. 13, Feb. 2019.

[4] J. Hannula, J. Holopainen, and V. Viikari, "Concept for Frequency-Reconfigurable Antenna Based on Distributed Transceivers," *IEEE Antennas and Wireless Propagation Letters*, vol. 16, pp. 764–767, 2017.

[5] R. Luomaniemi, J. Hannula, A. Lehtovuori, and V. Viikari, "Switch-Reconfigurable Metal Rim MIMO Handset Antenna With Distributed Feeding," *IEEE Access*, vol. 7, pp. 48 971–48 981, 2019.

[6] R. Martens and D. Manteuffel, "Systematic Design Method of a Mobile Multiple Antenna System Using the Theory of Characteristic Modes," *IET Microwaves, Antennas Propagation*, vol. 8, no. 12, pp. 887–893, 2014.

[7] N. Peitzmeier and D. Manteuffel, "Upper Bounds and Design Guidelines for Realizing Uncorrelated Ports on Multimode Antennas Based on Symmetry Analysis of Characteristic Modes," *IEEE Transactions on Antennas and Propagation*, vol. 67, no. 6, pp. 3902–3914, 2019.

[8] B. Yang and J. J. Adams, "Systematic Shape Optimization of Symmetric MIMO Antennas Using Characteristic Modes," *IEEE Transactions on Antennas and Propagation*, vol. 64, no. 7, pp. 2668–2678, 2016.

[9] (2021, May) 3rd Generation Partnership Project (3GPP) . 3GPP. [Online]. Available: https://www.3gpp.org/

[10] M. Capek, L. Jelinek, and M. Masek, "A Role of Symmetries in Evaluation of Fundamental Bounds," 2020.

[11] (2021, May) Antenna Toolbox for MATLAB (AToM). Czech Technical University in Prague. [Online]. Available: www.antennatoolbox.com

[12] (2021, May) CST Computer Simulation Technology. Dassault Systemes. [Online]. Available: http://www.cst.com/

[13] (2021, May) AWR Microwave Office. Cadence. [Online]. Available: web.awrcorp.com

[14] D. M. Pozar, *Microwave Engineering*, 3rd ed. Wiley, 2005.

[15] M. Manteghi and Y. Rahmat-Samii, "Multiport Characteristics of a Wide-band Cavity Backed Annular Patch Antenna for Multipolarization Operations," *IEEE Transactions on Antennas and Propagation*, vol. 53, no. 1, pp. 466–474, 2005.

[16] "IEEE Standard Definitions of Terms for Antennas," *IEEE Transactions on Antennas and Propagation*, vol. 17, no. 3, pp. 262–269, 1969.

[17] J. Volakis, C. C. Chen, and K. Fujimoto, *Small Antennas: Miniaturization Techniques and Applications*, 1st ed., W. C. Chew, M. S. Tong, and B. Hu, Eds. McGraw-Hill Professional, 2010.

[18] A. D. Yaghjian and S. R. Best, "Impedance, Bandwidth, and Q of Antennas," in *IEEE Antennas and Propagation Society International Symposium. Digest. Held in conjunction with: USNC/CNC/URSI North American Radio Sci. Meeting (Cat. No.03CH37450)*, vol. 1, 2003, pp. 501–504 vol.1.

[19] M. Capek, L. Jelinek, and M. Masek, "Finding Optimal Total Active Reflection Coefficient and Realized Gain for Multi-port Lossy Antennas," 2020.

[20] M. Wang, T. Loh, Y. Zhao, and Q. Xu, "A Closed-Form Formula of Radiation and Total Efficiency for Lossy Multiport Antennas," *IEEE Antennas and Wireless Propagation Letters*, vol. 18, no. 12, pp. 2468–2472, 2019.

[21] C. A. Balanis, *Antenna Theory: Analysis and Design*, 2nd ed. Wiley, 1996.

[22] A. Paulraj, R. Nabar, and D. Gore, *Introduction to Space-time Wireless Communications*. Cambridge University Press, 2003.

[23] A. F. Molisch, *Wireless Communications*, 2nd ed. Wiley, 2011.

[24] R. Harrington, "Reactively Controlled Directive Arrays," *IEEE Transactions on Antennas and Propagation*, vol. 26, no. 3, pp. 390–395, 1978.

[25] S. Rao, D. Wilton, and A. Glisson, "Electromagnetic Scattering by Surfaces of Arbitrary Shape," *IEEE Transactions on Antennas and Propagation*, vol. 30, no. 3, pp. 409–418, 1982.

[26] G. L. Nemhauser and L. A. Wolsey, *Integer and Combinatorial Optimization*, 1st ed., ser. Wiley Series in Discrete Mathematics and Optimization. Wiley, 1988.

[27] S. Boyd and L. Vandenberghe, *Convex Optimization*. Cambridge University Press, 2004.

[28] (2021, May) MATLAB. MathWorks. [Online]. Available: https://www.mathworks.com/products/matlab.html

[29] M. Masek, L. Jelinek, and M. Capek, "Excitation Schemes of Uncorrelated Channels," 2020.

[30] M. Gustafsson, M. Capek, and K. Schab, "Tradeoff Between Antenna Efficiency and Q-Factor," *IEEE Transactions on Antennas and Propagation*, vol. 67, no. 4, pp. 2482–2493, 2019.

[31] L. Jelinek, K. Schab, and M. Capek, "Radiation Efficiency Cost of Resonance Tuning," *IEEE Transactions on Antennas and Propagation*, vol. 66, no. 12, pp. 6716–6723, 2018.

[32] M. Capek, M. Gustafsson, and K. Schab, "Minimization of Antenna Quality Factor," *IEEE Transactions on Antennas and Propagation*, vol. 65, no. 8, pp. 4115–4123, 2017.

[33] L. Jelinek and M. Capek, "Optimal Currents on Arbitrarily Shaped Surfaces," *IEEE Transactions on Antennas and Propagation*, vol. 65, no. 1, pp. 329–341, 2017.

[34] D. Sánchez-Hernández, *Multiband Integrated Antennas for 4G Terminals*. Artech House, 01 2008.

[35] M. Capek, L. Jelinek, and M. Gustafsson, "Shape Synthesis Based on Topology Sensitivity," *IEEE Transactions on Antennas and Propagation*, vol. 67, no. 6, pp. 3889–3901, 2019.

[36] *Lead Free, Mid Tg Epoxy Laminate and Prepreg*, Isola, May 2021. [Online]. Available: https://www.isola-group.com/pcb-laminates-prepreg/is400/

[37] *HiQ-CBR Series, C0G Dielectric, Low ESR6.3 – 500 VDC, 1 MHz – 50 GHz (RF and Microwave)*, KEMET, May 2021. [Online]. Available: https://cz.mouser.com/datasheet/2/212/KEM_C1030_CBR_SMD-1101233.pdf

[38] *R&S ZVA Vector Network Analyzers*, Rohde & Schwarz, May 2021. [Online]. Available: https://www.rohde-schwarz.com/cz/product/zva-productstartpage_63493-9660.html

[39] A. Diallo, C. Luxey, G. Kossiavas, P. Besnier, A. Chousseaud, Y. Mahe, S. Toutain, B. Derat, C. Delaveaud, L. Robert, J. Carlsson, P.-S. Kildal, C. Orlenius, and O. Litschke, "Comparison of Efficiency Measurement Methods for Small Antennas," in *11th International Symposium on Antenna Technology and Applied Electromagnetics [ANTEM 2005]*, 06 2005, pp. 1–4.

[40] T. Vu, A. Diallo, C. Luxey, and G. Kossiavas, "Optimization of the Size and the Shape of a Wheeler Cap for Mobile Phone-Antenna Efficiency Measurements," in *The Second European Conference on Antennas and Propagation, EuCAP 2007*, 2007, pp. 1–6.

[41] R. F. Harrington, *Time-Harmonic Electromagnetic Fields*, 2nd ed. Wiley - IEEE Press, 2001.

[42] J. L. Volakis and K. Sertel, *Integral Equation Methods for Electromagnetics*. SciTech Publishing, 2012.

[43] W. C. Chew, M. S. Tong, and B. Hu, *Integral Equation Methods for Electromagnetic and Elastic Waves*, 1st ed., ser. Synthesis Lectures on Computational Electromagnetics. Morgan and Claypool Publishers, 2007.

[44] R. F. Harrington, *Field Computation by Moment Methods*, ser. The IEEE PRESS Series in Electromagnetic Waves (Donald G. Dudley, Editor). Wiley - IEEE Press, 1993.

[45] M. Gustafsson, D. Tayli, C. Ehrenborg, M. Cismasu, and S. Nordebo, "Antenna Current Optimization Using MATLAB and CVX," *Forum for Electromagnetic Research Methods and Application Technologies (FERMAT)*, Apr. 2016.

[46] M. Capek and L. Jelinek, "Optimal Composition of Modal Currents for Minimal Quality Factor q," *IEEE Transactions on Antennas and Propagation*, vol. 64, no. 12, pp. 5230–5242, 2016.

[47] M. Gustafsson and M. Capek, "Maximum Gain, Effective Area, and Directivity," *IEEE Transactions on Antennas and Propagation*, vol. 67, no. 8, pp. 5282–5293, 2019.

Appendix A

Electric Field Integral Equation and Its Solution

This appendix briefly reviews method-of-moments formulation of electric field integral equation. Time-harmonic steady-state is assumed at angular frequency ω with time convention $\partial/\partial t \to \mathrm{i}\omega$.

Consider scattering of an incident wave on a lossy conductor in vacuum. If losses are small, a surface equivalence principle might be employed on the boundary $\boldsymbol{r} \in \Omega$ of the conductor [41], leading to electric field integral equation

$$-\boldsymbol{n} \times \boldsymbol{n} \times \left(\mathcal{Z} \left\{ \boldsymbol{J} \left(\boldsymbol{r} \right) \right\} + \boldsymbol{E}^{\mathrm{i}} \left(\boldsymbol{r} \right) \right) = R_{\mathrm{s}} \left(\boldsymbol{r} \right) \boldsymbol{J} \left(\boldsymbol{r} \right), \tag{A.1}$$

where $\boldsymbol{n}$ is the unit normal to the boundary, $\boldsymbol{E}^{\mathrm{i}}$ is incident electrical field, $\boldsymbol{J}$ is equivalent surface current [42] and R_{s} is scalar function describing surface resistance. Loss model used throughout this work reads [14]

$$R_{\mathrm{s}} = \sqrt{\frac{\omega \mu_0}{2\sigma}}. \tag{A.2}$$

The operator $\mathcal{Z}$ in (A.1) is an impedance operator

$$\mathcal{Z} \left\{ \boldsymbol{J} \left(\boldsymbol{r} \right) \right\} = -\mathrm{i} k_0 Z_0 \int_{\Omega} \mathbf{G} \left(\boldsymbol{r}, \boldsymbol{r}' \right) \boldsymbol{J} \left(\boldsymbol{r}' \right) \mathrm{d}S', \tag{A.3}$$

where $\mathbf{G}$ is a free-space dyadic Green's function [43] with k_0 being the free space wave-number.

In order to solve (A.1) for the unknown current $\boldsymbol{J}$, method of moments is employed [44] by expansion into a series of basis functions $\boldsymbol{\psi}_n$ as

$$\boldsymbol{J} \left(\boldsymbol{r} \right) \approx \sum_{n=1}^{N} I_n \boldsymbol{\psi}_n \left(\boldsymbol{r} \right), \tag{A.4}$$

where I_n being the expansion coefficients of the unknown current density. Rao-Wilton-Glisson basis functions [25] are used throughout this work, see Figure A.1.

The expansion (A.4) together with Galerkin's testing and symmetric inner product convert operator equation (A.1) into

$$\mathbf{ZI} = \mathbf{V}, \tag{A.5}$$

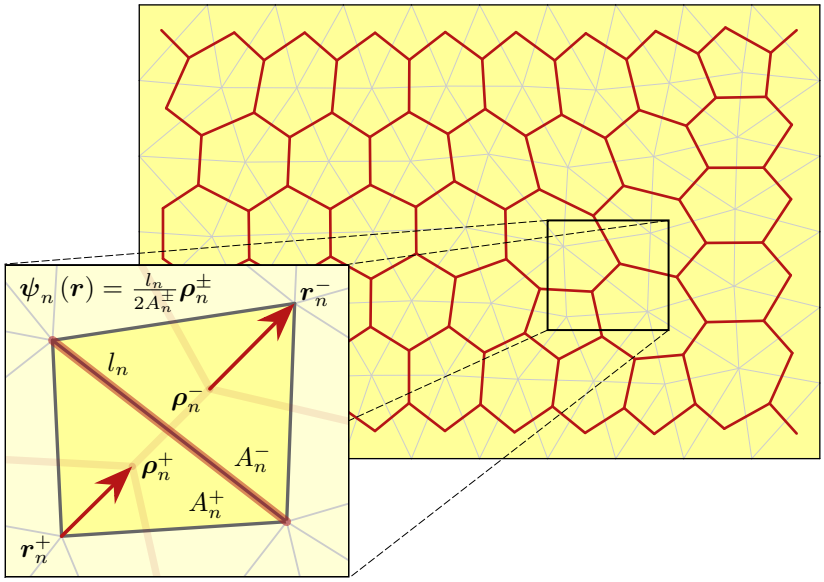

Figure A.1: RWG basis functions defined over triangular mesh. Meaning of symbols is same as in [25].

where $\mathbf{V}$ is feeding vector whose elements are evaluated as

$$V_n = \int_{\Omega} \boldsymbol{\psi}_n(\boldsymbol{r}) \cdot \boldsymbol{E}(\boldsymbol{r}) \, \mathrm{d}S. \tag{A.6}$$

Impedance matrix $\mathbf{Z}$ is further divided into its free-space part $\mathbf{Z}_0 = \mathbf{R}_0 + \mathrm{i}\mathbf{X}_0$ and loss part $\mathbf{R}_\rho$ with elements of the first one being obtained as

$$Z_{0,mn} = \mathrm{i}k_0 Z_0 \int_{\Omega}\int_{\Omega'} \boldsymbol{\psi}_m(\boldsymbol{r}) \cdot \mathbf{G}(\boldsymbol{r}, \boldsymbol{r}') \cdot \boldsymbol{\psi}_n(\boldsymbol{r}') \, \mathrm{d}S'\mathrm{d}S, \tag{A.7}$$

and the second one computed as

$$R_{\rho,mn} = R_\mathrm{s} \int_{\Omega} \boldsymbol{\psi}_m(\boldsymbol{r}) \cdot \boldsymbol{\psi}_n(\boldsymbol{r}) \, \mathrm{d}S. \tag{A.8}$$

Differentiating $\mathbf{Z}_0$ with respect to angular frequency ω leads to stored energy matrix [45]

$$\mathbf{W} = \mathrm{Im}\left\{\omega \frac{\partial \mathbf{Z}_0}{\partial \omega}\right\}, \tag{A.9}$$

used to evaluate stored electromagnetic energy [45] as

$$\omega W_\mathrm{sto} \approx \frac{1}{4}\mathbf{I}^\mathrm{H}\mathbf{W}\mathbf{I}, \tag{A.10}$$

Expansion (A.4) also allows for the definition of far-field vector $\mathbf{F}$ as evaluated as [33]

$$F_n(\hat{\boldsymbol{r}}, \hat{\boldsymbol{e}}) = -\frac{\mathrm{i}Z_0 k_0}{4\pi} \int_{\Omega} \hat{\boldsymbol{e}} \cdot \boldsymbol{\psi}_n(\boldsymbol{r}') \, \mathrm{e}^{\mathrm{i}k_0 \hat{\boldsymbol{r}} \cdot \boldsymbol{r}'} \mathrm{d}S, \tag{A.11}$$

which is used to evaluate partial radiation intensity as

$$U\left(\hat{\boldsymbol{r}},\hat{\boldsymbol{e}}\right)\approx\mathbf{I}^{\mathrm{H}}\mathbf{F}^{\mathrm{H}}\mathbf{F}\mathbf{I}. \tag{A.12}$$

.

Complex power conservation [30–32, 41, 46, 47] used to evaluate several antenna metrics in this thesis reads

$$P_{\mathrm{rad}}+P_{\mathrm{lost}}+\mathrm{i}P_{\mathrm{react}}=\frac{1}{2}\left\langle\boldsymbol{J}\left(\boldsymbol{r}\right),\mathcal{Z}\left\{\boldsymbol{J}\left(\boldsymbol{r}\right)\right\}\right\rangle\approx\frac{1}{2}\mathbf{I}^{\mathrm{H}}\mathbf{Z}\mathbf{I}, \tag{A.13}$$

where P_{rad} is radiated power, P_{lost} is dissipated power and P_{react} is reactive power.

Appendix B
Convergence of Solutions

This chapter focuses on various numerical aspects of results in this work. The use of structure symmetries in port placement is justified in Section B.1 while Sections B.2 and B.3 focus on the dependence of numerical results on used discretization and on comparison with commercially available solvers. Everything is observed on impedance and admittance parameters because every other figure of merit is dependent on them.

B.1 Reduction of Symmetrical Solutions

Antenna model, see Figure 1.1, exhibits symmetries with respect to mirroring by xz plane and yz plane and rotation by 180 degrees around axis z. Utilizing this, solution space to port placement optimization can accordingly be reduced. However, the used discretized model does not preserve these symmetries, see Figure 1.2. This section shows that for dense enough mesh, the chosen approach is nonetheless precise approximation. The ϵ-function is used as a measure of difference between two solutions

$$\epsilon_n(\xi) = \left| \frac{\xi_1 - \xi_n}{\xi_1} \right| \quad n = 2, 3, 4, \tag{B.1}$$

with ξ representing chosen quantity and n being indices of particular feeding region from Ω_2 to Ω_4, see inset in Figure B.1. Reference port position is set to a particular place in region Ω_1 and then symmetrically placed port from one of regions Ω_2 to Ω_4 is examined.

Input impedance is used as the studied quantity, see Figures B.1. The maximal relative difference between solutions is lower than 0.01 for both parts. The error between various solutions is negligible, and reduction of solution space solely to region Ω_1 of port placement is valid.

B.2 Numerical Convergence

A large set of frequencies has to be evaluated to capture the frequency dependence of total active reflection coefficient Γ^{t}. This operation takes a considerable amount of computational time, which grows fast with the

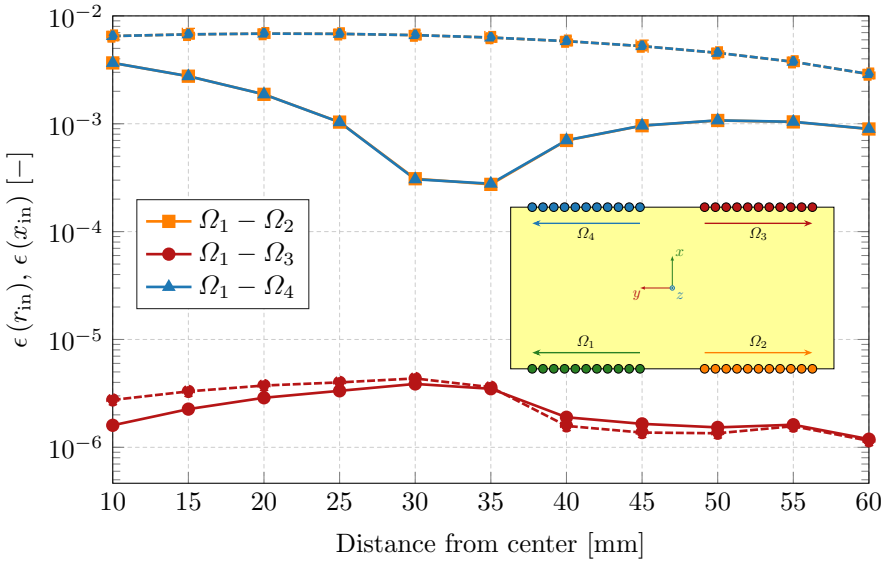

Figure B.1: Epsilon function applied for input impedance. The solid line represents r_{in} and the dashed line is x_{in}. Inset shows structure with the indicated direction of distance from the center. Markers in the inset denote reviewed port positions, with green markers in inset denoting reference port region.

number of discretization elements and the order of numerical quadratures used to evaluate reaction integrals. High quadrature and a high number of discretization elements is however desired for the accuracy of the results. There is, therefore, a trade-off between achieved accuracy and computational time. Total efficiency η_{tot} is exceptionally evaluated without parallel tuning element and with feeding line impedance fixed to $R_{\text{c}} = 50\,\Omega$. The 1-port antenna is examined.

Let us start with a fixed number of basis functions $N = 1248$ and let us observe the effect of quadrature order q on the accuracy of the several antenna metrics[1] for defined in 2.1 evaluated for the 1-port antenna. The results are shown in Table B.1. It can be seen that for the particular setup used in this thesis, the quadrature order q does not have a serious impact on resulting figures of merits.

Next, the effect of discretization density on accuracy is studied in Table B.2 for a fixed quadrature order $q = 5$. Discretization of the metallic rim for the first three discretizations from Table B.2, *i.e.*, $N = \{1248, 3300, 5460\}$ is shown in Figure B.2. Ground plane is discretized with Delaunay triangulation and it has 562 triangles for first row of Table B.2 and 1660 triangle for the rest four rows.

It is observed that results become convergent at two significant digits for all observed metrics when the number of basis function exceeds $N = 5000$. The highest discrepancies are in x_{in}, which is expected, as reactance depends not only on the overall current shape but also on the details of the feeding

[1] Directivity is evaluated as sum of $\hat{\boldsymbol{\theta}}$ and $\hat{\boldsymbol{\varphi}}$ polarizations at the direction $\theta = 180°$ and $\varphi = 0°$.

q [−]	r_{in} [Ω]	x_{in} [Ω]	η_{tot} [−]	η_{rad} [−]	Q [−]	D [−]
2	12.64	36.22	0.4509	0.9336	53.11	2.533
3	12.62	36.77	0.4468	0.9335	53.29	2.534
4	12.44	37.27	0.4388	0.9323	54.07	2.541
5	12.41	37.37	0.4372	0.9321	54.25	2.542
6	12.38	37.57	0.4352	0.9319	54.39	2.543

Table B.1: Results dependence on quadrature order.

region.

N [−]	r_{in} [Ω]	x_{in} [Ω]	η_{tot} [−]	η_{rad} [−]	Q [−]	D [−]
1248	12.41	37.37	0.4372	0.9321	54.21	2.542
3300	12.23	33.58	0.4546	0.9292	53.59	2.535
5460	12.29	27.81	0.4846	0.9172	51.99	2.527
7620	12.33	26.75	0.4888	0.9118	51.71	2.527
8700	12.35	26.55	0.4894	0.9099	51.64	2.527

Table B.2: Results dependence on number of discretization elements.

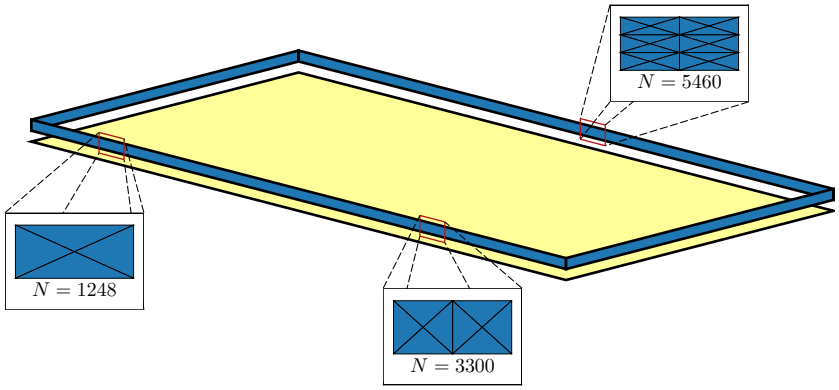

Figure B.2: Triangle elements between two ports with various mesh densities.

This work uses mesh grid consisting of $N = 1248$ basis functions with quadrature order of $q = 4$. Although it is not optimal for the accuracy of results, it serves well to describe qualitative trends.

B.3 Comparison with Commercial Software

This section provides cross-validation, on port admittance matrices, of the results obtained with the in-house tool AToM [11] used in this thesis and results obtained with commercial simulator CST [12]. The validation starts with input admittance of a 1-port antenna, see Figure B.3. A shift of resonance frequency by approximately one percent can be observed. The overall shape and span of corresponding curves also show great similarity. Mesh structure used in AToM consists of 922 triangles, and mesh structure in CST consists of 920 triangles. Although the number of triangles is almost the same, the resulting discretization is different.

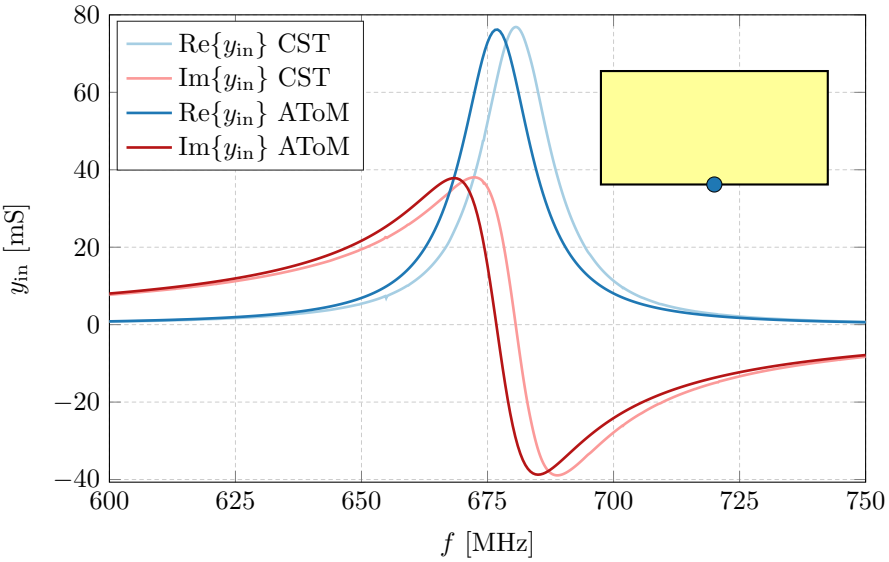

Figure B.3: Input admittance comparison. Inset show position of examined port.

The case of the 2-port antenna is shown in Figure B.4. Diagonal elements of admittance matrices are equal, and, therefore, only elements y_{11} and y_{12} are shown. Mesh structure used for simulation in AToM consists again of 922 triangles, and mesh structure used for simulation in CST consists of 1380 triangles. Same as in the previous case, it can be seen that although the resulting curves have a slight frequency shift, the overall shape of the curves is almost identical.

This section together with Section B.2 show rightness of simulations results. Although better precision could be achieved with a higher number of discretization elements, all results evaluated in previous sections are based on reasonably large mesh structures to achieve a quick preview on structure performance. Matching elements has to be slightly modified when an accurate physical model is used anyway.

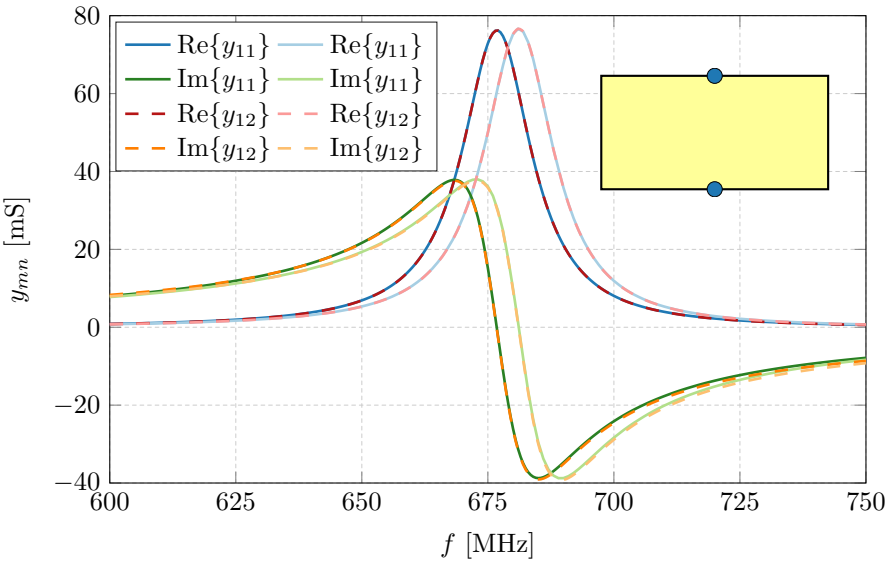

Figure B.4: Admittance matrices comparison. Dark colors are used for AToM results and light colors are used for CST results. Inset shows port positions of examined 2-port antenna.